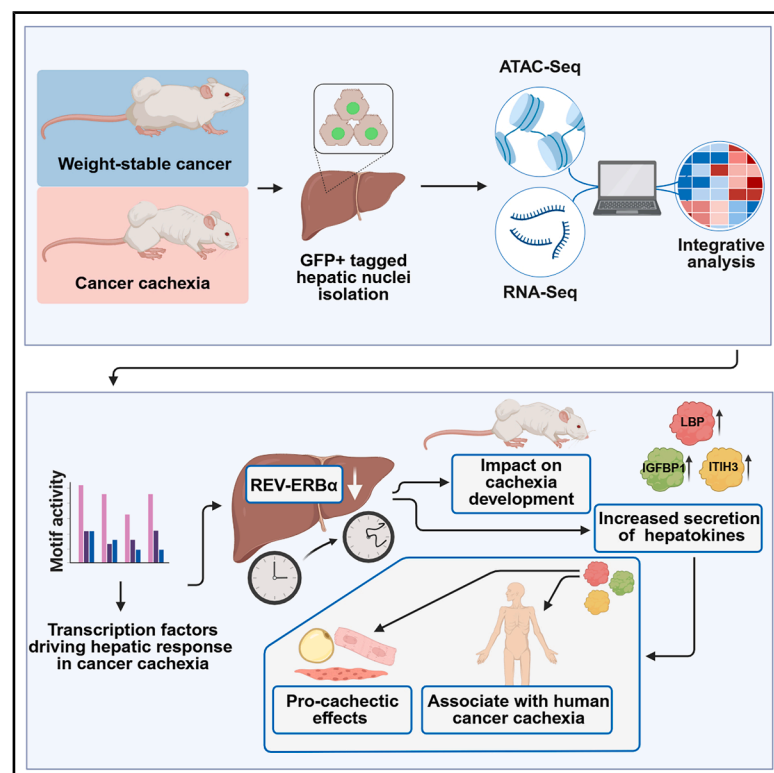


Functional liver genomics identifies hepatokines promoting wasting in cancer cachexia

Graphical abstract



Authors

Doris Kaltenecker, Søren Fisker Schmidt, Peter Weber, ..., Johannes Backs, Stephan Herzig, Mauricio Berriel Diaz

Correspondence

stephan.herzig@helmholtz-munich.de (S.H.), mauricio.berrieldiaz@helmholtz-munich.de (M.B.D.)

In brief

Cancer-induced liver changes promote body wasting through secreted factors, with circadian regulators and hepatokines being important contributors to cancer cachexia.

Highlights

- Cancer cachexia induces pronounced transcriptional changes in hepatocytes
- Dysregulated circadian clock components are drivers of transcriptional reprogramming
- Hepatic overexpression of REV-ERB α ameliorates tissue wasting in cancer cachexia
- Cachexia-induced hepatokines contribute to tissue wasting

Article

Functional liver genomics identifies hepatokines promoting wasting in cancer cachexia

Doris Kaltenecker,^{1,2,3,21} Søren Fisker Schmidt,^{1,2,3,4,21} Peter Weber,^{1,2,3} Anne Loft,^{1,2,3,4} Pauline Morigny,^{1,2,3} Juliano Machado,^{1,2,3} Julia Geppert,^{1,2,3} Kerstin Beate Saul,^{5,6,7} Pia Benedikt,^{1,2,3} Claudia-Eveline Molocea,^{1,2,3} Rachel Scott,^{8,9} Kerstin Haase,^{8,9} Marc E. Martignoni,¹⁰ Ana Jimena Alfaro,^{1,2,3} Kan Kau Chow,^{1,2,3} Estefania Simoes,^{1,2,3,11} José Pinhata Otoch,¹¹ Joanna D.C.C. Lima,¹¹ Charles Swanton,^{8,12,13} Nadine Spielmann,¹⁴ Martin Hrabé de Angelis,¹⁴ Markus Elsner,¹⁵ Ali Ertürk,^{15,16,17} Kenneth A. Dyar,^{1,3} Maria Rohm,^{1,2,3} Olga Prokopchuk,¹⁰ Mariam Jamal-Hanjani,^{8,9,12} Marilia Seelaender,¹¹ Johannes Backs,^{5,6,7,18,19} Stephan Herzig,^{1,2,3,20,*} and Mauricio Berriel Diaz^{1,2,3,22,*}

¹Institute for Diabetes and Cancer (IDC), Helmholtz Munich, German Research Center for Environmental Health, 85764 Neuherberg, Germany

²Joint Heidelberg-IDC Translational Diabetes Program, Heidelberg University Hospital, 69120 Heidelberg, Germany

³German Center for Diabetes Research (DZD), 85764 Neuherberg, Germany

⁴Department of Biochemistry and Molecular Biology, Center for Functional Genomics and Tissue Plasticity (ATLAS) and Functional Genomics & Metabolism Research Unit, University of Southern Denmark, 5230 Odense, Denmark

⁵Heidelberg University, Medical Faculty Heidelberg, Institute of Experimental Cardiology, 69120 Heidelberg, Germany

⁶Heidelberg University Hospital, Department of Internal Medicine VIII, 69120 Heidelberg, Germany

⁷German Center for Cardiovascular Research (DZHK), Partner Site Heidelberg/Mannheim, 69120 Heidelberg, Germany

⁸Cancer Research UK Lung Cancer Centre of Excellence, University College London Cancer Institute, WC1E 6BT London, UK

⁹Cancer Metastasis Laboratory, University College London Cancer Institute, WC1E 6DD London, UK

¹⁰Department of Surgery, Klinikum Rechts der Isar, School of Medicine, Technical University of Munich, 81675 Munich, Germany

¹¹Cancer Metabolism Research Group, LIM 26 HC, Medical School, University of São Paulo, 01246-904 São Paulo, Brazil

¹²Department of Oncology, University College London Hospitals, NW1 2PB London, UK

¹³Cancer Evolution and Genome Instability Laboratory, The Francis Crick Institute, NW1 1AT London, UK

¹⁴Institute of Experimental Genetics, German Mouse Clinic, Helmholtz Munich, 85764 Neuherberg, Germany

¹⁵Institute for Intelligent Biotechnologies, Helmholtz Munich, 85764 Neuherberg, Germany

¹⁶Institute for Stroke and Dementia Research, Klinikum der Universität München, Ludwig-Maximilians University Munich, 81377 Munich, Germany

¹⁷School of Medicine, Koç University, 34450 İstanbul, Turkey

¹⁸Molecular Medicine Partnership Unit, Heidelberg University, 69120 Heidelberg, Germany

¹⁹Helmholtz Institute for Translational AngioCardioScience (HI-TAC)—a branch of the MDC at Heidelberg University, 69120 Heidelberg, Germany

²⁰Molecular Metabolic Control, TU Munich, Munich, Germany

²¹These authors contributed equally

²²Lead contact

*Correspondence: stephan.herzig@helmholtz-munich.de (S.H.), mauricio.berrieldiaz@helmholtz-munich.de (M.B.D.)

<https://doi.org/10.1016/j.cell.2025.06.039>

SUMMARY

In cancer cachexia, the presence of a tumor triggers systemic metabolic disruption that leads to involuntary body weight loss and accelerated mortality in affected patients. Here, we conducted transcriptomic and epigenomic profiling of the liver in various weight-stable cancer and cancer cachexia models. An integrative multi-level analysis approach identified a distinct gene expression signature that included hepatocyte-secreted factors and the circadian clock component REV-ERB α as key modulator of hepatic transcriptional reprogramming in cancer cachexia. Notably, hepatocyte-specific genetic reconstitution of REV-ERB α in cachexia ameliorated peripheral tissue wasting. This improvement was associated with decreased levels of specific cachexia-controlled hepatocyte-secreted factors. These hepatokines promoted catabolism in multiple cell types and were elevated in cachectic cancer patients. Our findings reveal a mechanism by which the liver contributes to peripheral tissue wasting in cancer cachexia, offering perspectives for future therapeutic interventions.

INTRODUCTION

Cancer has the capacity to trigger profound changes in the patient's systemic metabolism. This phenomenon is especially

obvious in the context of cancer cachexia (CCx), a multifactorial syndrome characterized by the involuntary and substantial loss of body weight. Depending on the tumor type, 50%–80% of cancer patients suffer from CCx.^{1,2} It is caused by a combination of

systemic inflammation, elevated energy expenditure, increased catabolism and loss of appetite, induced by tumor- and host-derived factors.^{3–5} CCx leads to progressive functional impairments, poor quality of life, increased toxicity to chemotherapy, and increased mortality.^{3,4} CCx accounts for at least 20% of cancer-related deaths,² and currently, there is no Food and Drug Administration (FDA)-approved treatment that can completely reverse it.^{1,3}

Increased circulating levels of various tumor-derived proteins have been proposed as mediators of CCx. These factors either directly drive catabolic processes in key target tissues, such as muscle and adipose tissue, or trigger host responses that contribute to systemic wasting.⁶ Specific cytokines, including interleukin (IL)-6, growth differentiation factor 15, and leukemia inhibitory factor are thought to play a central role in the etiology of CCx, potentially distinguishing CCx from weight-stable cancer states.⁶

While a plethora of studies focused on elucidating mechanisms that govern wasting processes in skeletal muscle and adipose tissue, less attention has been paid to the contribution of the liver.⁷ CCx is associated with the activation of the hepatic acute-phase response,^{8,9} which might contribute to muscle loss by a shift of amino acid usage.^{7,10} Additionally, the liver is thought to increase energy expenditure in CCx through futile metabolic cycles that do not serve anabolic or energy-generating functions.¹¹ Recent studies also connected CCx with changes in liver function and inflammation.^{12–17} However, molecular insights into hepatocyte-specific changes in CCx and how they differ from weight-stable cancers remain limited, and whether hepatocyte-secreted proteins contribute to systemic tissue wasting is unclear.

Here, using transcriptomic and epigenomic profiling of hepatocytes from different mouse models of weight-stable cancer and CCx, we discovered a cachectic gene expression signature comprising dysregulated circadian clock components as primary drivers of the transcriptional remodeling observed in CCx. By manipulating hepatic REV-ERB α (nuclear receptor subfamily 1 group D member 1, NR1D1), a master-regulator of the circadian clock, we were able to ameliorate muscle and adipose tissue loss in CCx. Hepatokines regulated by REV-ERB α triggered cachexia-typical catabolic processes in target cells including myotubes. In patients with cachexia, these hepatocyte-secreted factors were also increased, compared with patients with weight-stable cancer.

RESULTS

Profiling of the liver transcriptome identifies cachexia-associated programs

To study hepatocyte-specific changes in CCx, we isolated nuclei from hepatocytes of different mouse models of weight-stable cancer and CCx using the “isolation of nuclei tagged in specific cell types” (INTACT) methodology. INTACT allows for Cre-lox-driven cell-type-specific labeling and subsequent affinity purification of nuclei from INTACT tissues.^{18,19}

We implanted cachexia-inducing cancer cells (C26 colon cancer and 8025 pancreatic ductal adenocarcinoma [PDAC]) or cancer cells that give rise to weight-stable cancer (NC26 and MC38

colon cancer cells) into syngeneic hepatocyte INTACT (HEP-INTACT) mice, which express the nuclear tag (sun1 sfGFP Myc) specifically in hepatocytes. BALB/c or C57BL/6 background were used depending on the cancer cell lines (Figure 1A).

As expected,^{20,21} cachectic C26 (C26_Cx) and PDAC 8025 tumor-bearing mice displayed significant body weight losses compared with PBS controls (Figures 1B, S1A, and S1J), along with reduced weights of gastrocnemius (GC) muscle, epididymal white adipose tissue (eWAT), and subcutaneous (sc) WAT (Figures S1B–S1G and S1K). We also included pre-cachectic C26 tumor-bearing mice (C26_pre-Cx) that displayed no significant changes in body weight compared with PBS controls (Figures 1B and S1A), representing a state preceding wasting. In this group, the tumor weights were lower than in cachectic C26 tumor-bearing mice (Figures S1A–S1G). By contrast, NC26 and MC38 tumor caused no significant changes in body or tissue weights (Figures 1B, S1H, S1I, S1L, and S1M), confirming the weight-stable nature of these cancer models.^{21,22}

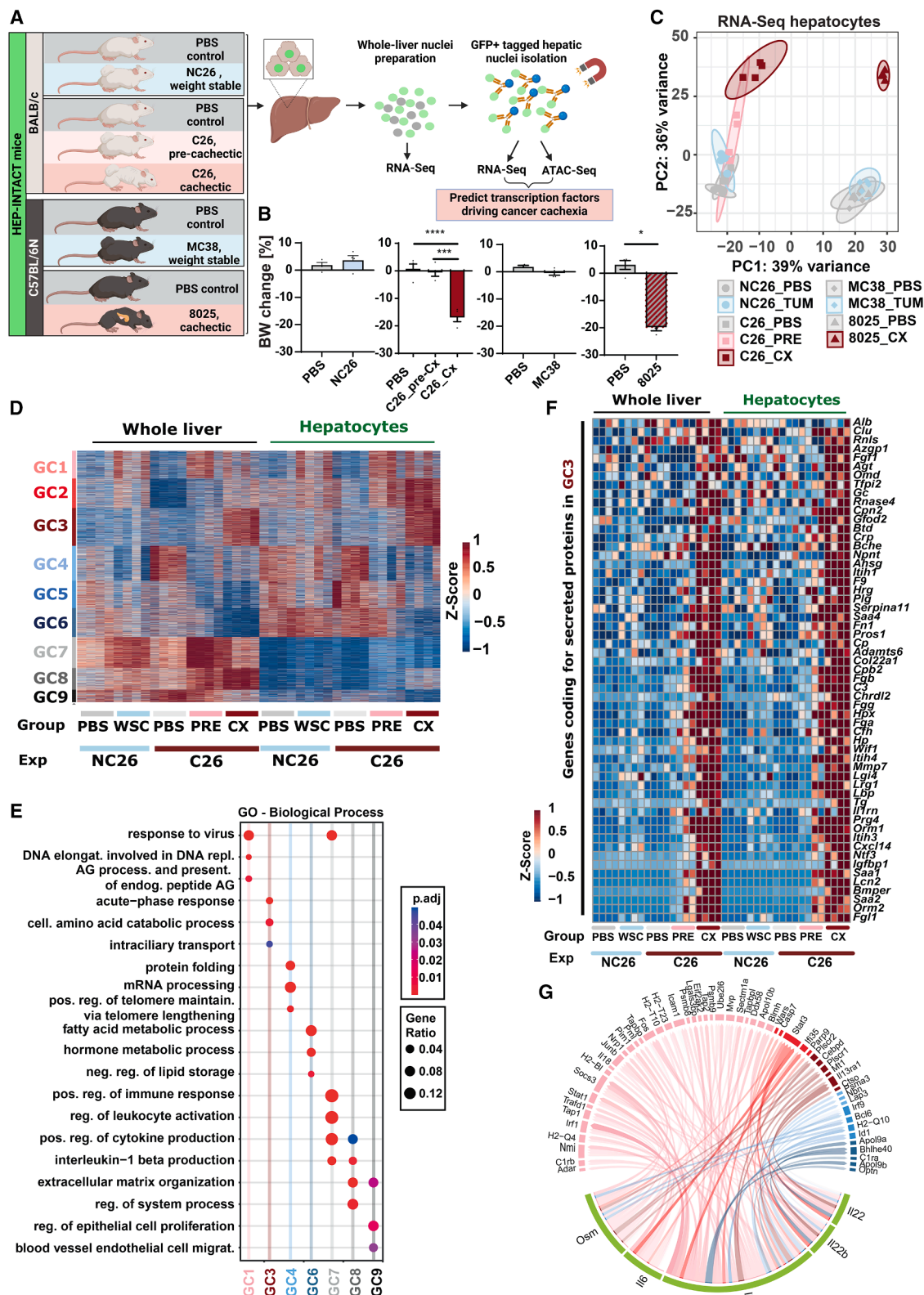
We isolated nuclei from these mice and performed RNA sequencing (RNA-seq) on both whole-liver and GFP+ hepatocyte nuclei and assay for transposase-accessible chromatin sequencing (ATAC-seq) on hepatocyte nuclei (Figure 1A).

Principal-component analyses (PCA) and correlation analyses showed that weight-stable tumor groups (NC26 and MC38) showed few overall changes compared with PBS-injected controls (Figures 1C and S1N–S1R). By contrast, both cachexia models (C26 and 8025) displayed substantial and distinct alterations in their expression and ATAC-seq profiles, with the pre-cachectic group showing an intermediate profile between the control and the fully cachectic groups (Figures 1C, S1N, and S1O).

As expected,²³ hepatocyte marker genes were enriched in GFP+ nuclei compared with whole-liver nuclei, which conversely displayed higher expression of marker genes for non-parenchymal liver resident and inflammatory cell types (Figures 1S and 1T).

To unravel the hepatic transcriptional response to cachexia progression, we initially focused on the data from our C26 model, which included a pre-cachexia time point, and the corresponding weight-stable NC26 model. We identified 5,534 genes that were significantly altered between one or more conditions in either GFP+ nuclei or whole-liver nuclei and subjected these to K-means clustering (Figure 1D). We identified nine gene clusters (GC1–GC9). Six of these displayed an increased signal in purified hepatocyte nuclei (GC1–GC6), whereas genes in the remaining three (GC7–GC9) were primarily expressed in whole-liver nuclei. Consistently, these clusters showed similar expression changes relative to PBS-injected mice in the two complementary models of weight-stable (MC38) and cachectic cancer (8025), including an induction of gene cluster 3 (GC3) in cachectic mice (Figure S2A).

Gene Ontology (GO) pathway analyses identified functional categories that were enriched in individual clusters (Figure 1E). Genes activated in hepatocytes during cachexia progression (GC3) were enriched in amino acid metabolism/catabolic processes and acute-phase response pathways, whereas cachexia progression was associated with repression of hepatocyte genes involved in protein folding (GC4) and fatty acid



(legend on next page)

metabolism (GC6). Genes with increased expression in whole-liver nuclei containing also nuclei from non-parenchymal cells (NPCs) showed enrichment in terms related to immune processes and extracellular matrix organization (GC8), whereas cachexia repressed genes appear to be involved in endothelial cell migration (GC9). In line with these pathway analyses, we found that particularly GC3 and GC8 contained many genes encoding secreted proteins (Figure S2B). Furthermore, GC3 contained genes coding for well-known secreted acute-phase response proteins such as serum-amyloid A1 and A2 (*Saa1* and *Saa2*), alpha-1-acid glycoprotein 1–3 (*Orm1*, *Orm2*, and *Orm3*) and fibrinogen (*Fga*, *Fgb*, and *Fgg*) (Figure 1F). Using NicheNet,²⁴ we performed interaction predictions between ligands and their putative target genes in gene regulatory networks to uncover potential upstream regulators of gene program alterations in CCx within hepatocytes and whole-liver nuclei (Figures 1G and S2C). In hepatocytes, this analysis highlighted pro-cachectic IL-6, Oncostatin M (OSM), IL-27, IL-22, and IL-22b as primary upstream modulators. In whole-liver nuclei, in addition to numerous interleukins, we identified tumor necrosis factor alpha (TNF- α) and interferon gamma as factors previously linked to CCx²⁵ as regulators of gene expression changes.

Collectively, we show that the transcriptional response in hepatocytes in CCx is distinct compared with weight-stable cancer, spanning various tumor models. Furthermore, our analysis demonstrates a notable upregulation of genes encoding secreted proteins in hepatocytes, suggesting a potential avenue through which hepatocytes affect cachexia progression.

Analysis of enhancer and transcription factor dynamics identify REV-ERB α as modulator of the cachectic response in hepatocytes

To understand the regulatory mechanisms underlying the changes in gene expression observed in hepatocytes during cachexia progression, we next analyzed our ATAC-seq data from GFP+ nuclei isolated from the livers of control and tumor-bearing mice. Focusing initially on the C26 and NC26 models, we identified 13,906 enhancers with significant changes in chromatin accessibility between one or more conditions in GFP+ nuclei and subjected these to K-means clustering (Figure 2A). We identified four enhancer clusters (ECs) with distinct temporal profiles, and the effect of weight-stable cancer and cachexia was generally conserved in the MC38 and

8025 models (Figure S2D). These ECs were enriched near genes from expression clusters with similar temporal activation patterns during cachexia progression (Figure 2B), exemplified by the *Orm2/3*, *Igf1bp1*, *Fabp1*, and *Ces1f* loci (Figures 2C and S2E). In these instances, late gene activation during cachexia correlated with a late increase in chromatin accessibility at nearby enhancers (EC2) (Figure 2C), or repression during cachexia with reduced accessibility at nearby enhancers (EC3 and EC4) (Figure S2E).

To identify the transcription factors that drive the gene expression changes observed in hepatocytes during cachexia pathogenesis, we used the "integrated analysis of motif activity and gene expression changes of transcription factors" (IMAGE) machine learning approach to predict which transcription factor motifs are contributing to the observed changes in transcriptional activity (regulatory motif activities).²⁶ Focusing initially on the C26 and NC26 models, we identified 98 motifs that significantly changed in activity between one or more conditions in GFP+ hepatocyte nuclei (Figure 2D). These grouped into four motifs clusters (MCs) that generally showed similar regulatory trends in our with C57BL/6N background with ECs 2 and 4 showing the clearest and most consistent association with cachexia progression (Figure S2F).

The motifs in cluster 2 displaying high increase in activity in cachexia included motifs recognized by transcription factors that are linked to inflammatory responses such as signal transducer and activator of transcription (STAT) 3 and the glucocorticoid receptor (GR, encoded by *Nr3c1*) (Figure 2E). Transcription factors with decreased motif activity in cachexia included hepatocyte identity factors such as the nuclear receptors ONECUT1 and NR1H3 (Figure S2G).

Notably, two of the top scoring motifs in MC2 were NR1D2 and RORC (Figure 2E). These are linked to two nuclear hormone receptor families, the REV-ERBs and the retinoic orphan related receptors (RORs) that are key members of the circadian clock and bind highly similar motifs (Figure 3A). The circadian clock regulates the expression of its target genes in a circadian manner with 24-h periodicity controlling physiologic homeostasis.²⁷ It is composed of interlocking transcriptional and translational feedback loops. A heterodimer of transcriptional activators brain and muscle ARNT-like 1 (BMAL1, encoded by *Arntl1*) and circadian locomotor output cycles kaput drive rhythmic gene expression. Among targets are the nuclear receptors

Figure 1. Temporal dynamics of the hepatic transcriptome in cancer cachexia

(A) Experimental pipeline: hepatocyte INTACT (HEP-INTACT) BALB/c or C57BL/6N mice with GFP labeled hepatic nuclei were implanted with cancer cell lines that give rise to weight-stable cancer (subcutaneous [s.c.] injection of NC26 and MC38 colon cancer cells) or cancer-associated weight loss (s.c. injection of C26 colon cancer cells, orthotopic implantation of 8025 pancreatic cancer cells). Control mice were injected subcutaneously or orthotopically with PBS. RNA sequencing was performed on nuclei of whole livers and enriched hepatic nuclei. Hepatic nuclei were also used for ATAC sequencing.

(B) Body weight changes ($n = 4/\text{group}$, error bars indicate standard error of the mean; ANOVA and Sidák's multiple comparisons test for C26 model; Mann-Whitney test for 8025 model. * $p < 0.05$, *** $p < 0.001$, **** $p < 0.0001$).

(C) Principal-component analysis of RNA-seq data of hepatocytes. NC26_PBS, C26_PBS, MC38_PBS, 8025_PBS represent non-tumor-bearing PBS-injected control to the respective tumor model. TUM, tumor.

(D) K-means clustering of row-scaled expression of genes differentially expressed ($p_{\text{adj}} < 0.05$, DESeq2) between one or more conditions in weight-stable cancer (WSC, NC26) or in cancer cachexia (CCx, C26) models in either whole-liver nuclei or GFP+ nuclei from HEP-INTACT mice. GC, gene cluster.

(E) Functional enrichment analysis using Gene Ontology biological processes for the indicated GCs.

(F) Heatmap showing row-scaled expression of genes encoding secreted proteins within gene cluster 3.

(G) NicheNet analysis of ligand-target connections in hepatocytes during cachexia. CX, cachexia; WSC, weight-stable cancer.

See also Figures S1 and S2.

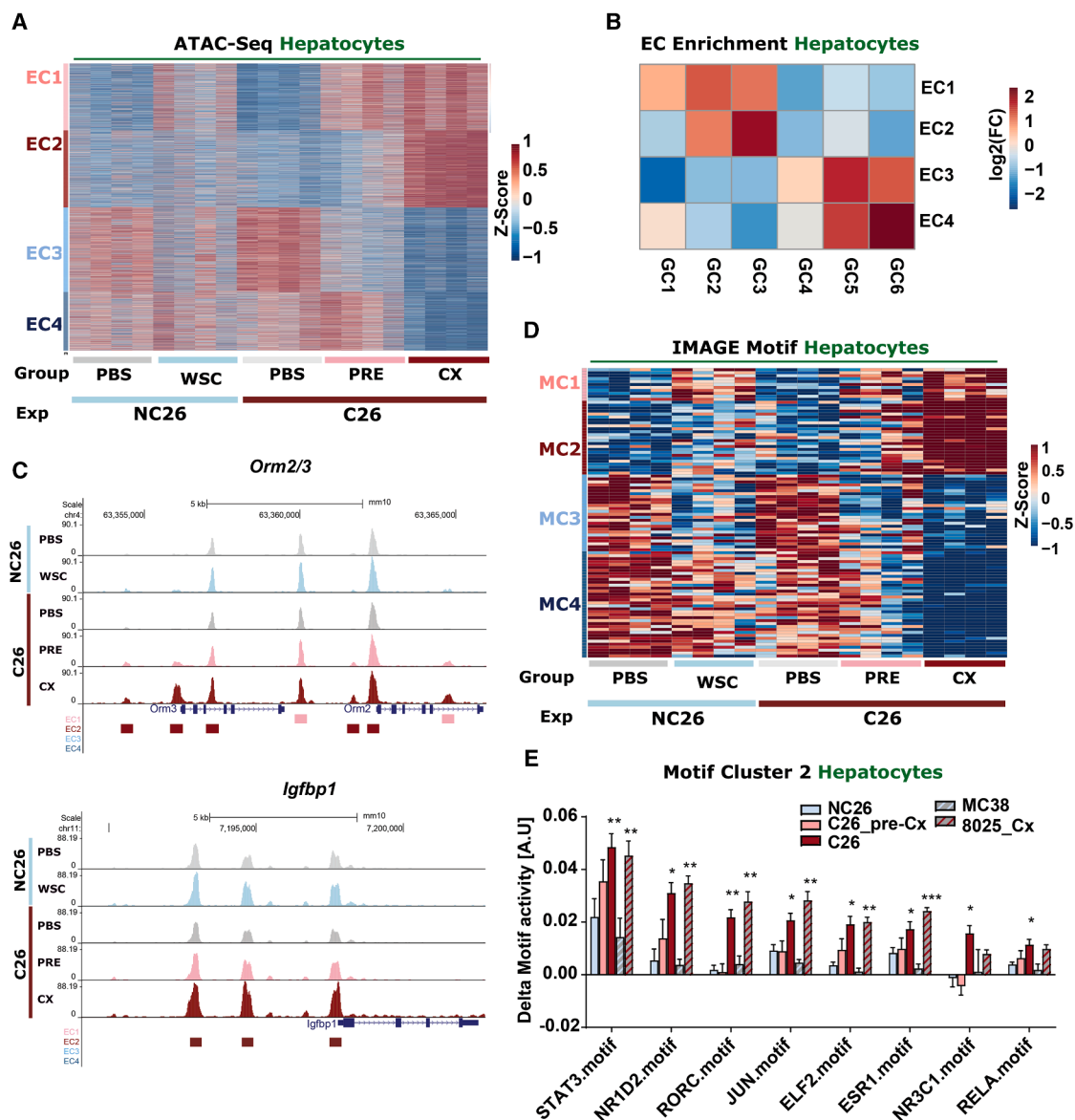


Figure 2. Enhancer and transcription factor dynamics driving the hepatocyte response to cachexia

(A) K-means clustering of row-scaled ATAC-seq tag counts within enhancers differentially accessible ($p_{\text{adj}} < 0.05$, DESeq2) between one or more conditions (BALB/c models) in GFP+ nuclei from HEP-INTACT mice. EC, enhancer cluster.
(B) Enrichment of enhancer clusters (EC1–EC4) defined in (A) in the vicinity (20 kb from TSS) of genes in the gene clusters (GCs) defined in Figure 1D. Log₂ enrichment is calculated relative to the number of enhancers in the vicinity of non-regulated, expressed genes.
(C) UCSC genome browser screenshots showing ATAC-seq read density in the orosomucoid 2/3 (*Orm2/3*) and insulin-like growth factor-binding protein 1 (*Igfbp1*) locus in GFP+ nuclei from HEP-INTACT mice. Average profiles ($n = 3–4$) of the indicated conditions are shown.
(D) K-means clustering of row-scaled IMAGE-predicted activities of differentially active transcription factor motifs ($p_{\text{adj}} < 0.05$, two-tailed t test corrected by the Benjamini and Hochberg method) between one or more conditions (BALB/c models) in GFP+ nuclei from HEP-INTACT mice. MC, motif cluster.
(E) Averaged changes in motif activity (relative to PBS) for the top 8 predicted transcription factors with cachexia-induced motif activities in motif cluster 2 ($n = 4/\text{group}$). Error bars indicate standard error of the activity-difference estimated with t test. * $p < 0.05$, ** $p < 0.01$, *** $p < 0.001$. CX, cachexia; WSC, weight-stable cancer; NR3C1, glucocorticoid receptor; RELA, RELA proto-oncogene, NF- κ B subunit.
See also Figure S2.

REV-ERB α and β (encoded by *Nr1d1* and *Nr1d2*, respectively), which function as transcriptional repressors. REV-ERB α / β compete with RORs (encoded by *Rora*, *Rorb*, and *Rorc*) in promoter binding and inhibit *Arntl1* expression. Thereby, REV-

ERBs form a negative feedback loop that sustains the rhythmicity of the system.^{27,28}

Of the five transcription factors in these two identified families (RORs and REV-ERBs), the most drastic alteration in gene

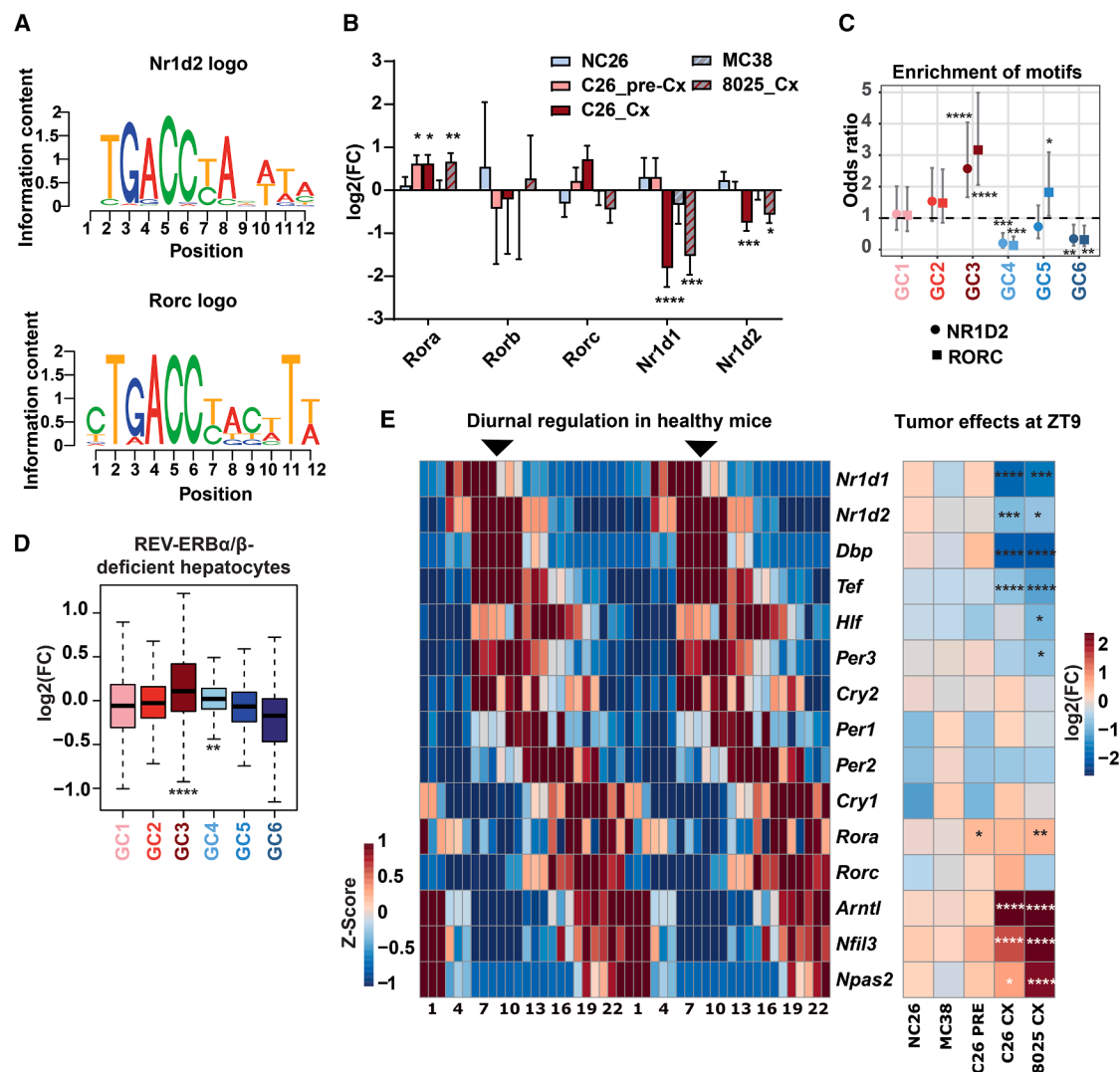


Figure 3. Cachexia promotes alterations in the hepatocyte core clock

(A) Sequence logos of the NR1D2 and RORC motifs identified by IMAGE as top cachexia-activated motifs from Figure 2E.

(B) Expression changes of genes encoding transcription factors in the ROR and NR1D families. DESeq2-estimated log₂FC and standard error relative to PBS are depicted for the indicated tumor models.

(C) Enrichment of IMAGE-predicted target genes of the NR1D2 and RORC motif within the gene cluster (GC1–GC6) identified in Figure 1D. Error bars indicate the 95% confidence interval (Fisher exact test).

(D) Expression changes induced by hepatocyte-specific REV-ERBα/β deficiency of genes in the six hepatocyte GCs identified in Figure 1D. Error bars indicate 1.5 times of the inter-quartile range.

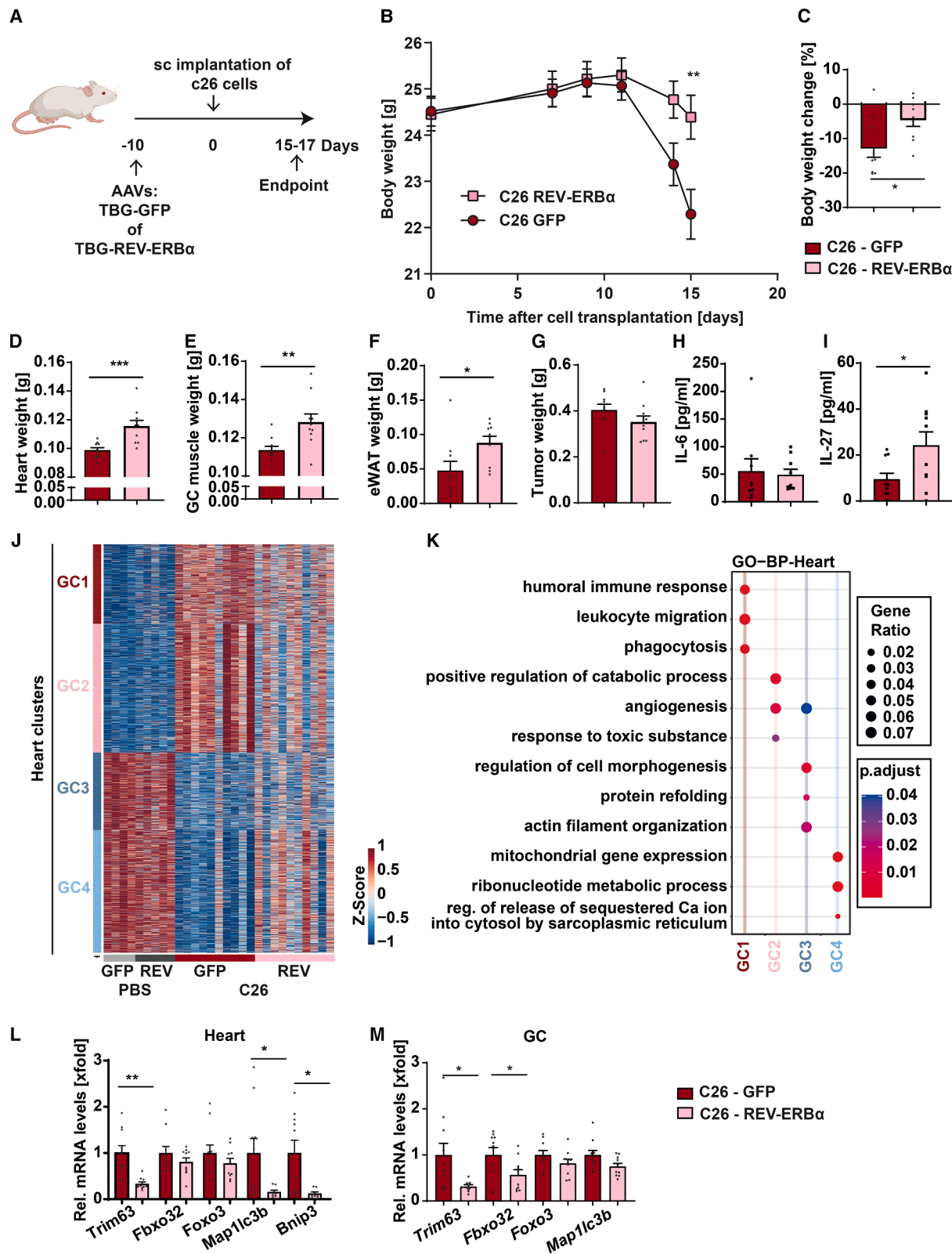
(E) Heatmaps showing diurnal expression of core clock genes in healthy mice (left) and expression changes of these genes in the depicted tumor models (right, this study, DESeq2 analysis). Genes are ordered according to their diurnal peak expression in healthy mice (left). **p* < 0.05, ***p* < 0.01, ****p* < 0.001, *****p* < 0.0001. CX, cachexia.

expression was observed for *Nr1d1* (encoding REV-ERBα) in cachectic mice, followed by *Nr1d2* (encoding REV-ERBβ) (Figure 3B). Reduced REV-ERBα expression was confirmed at the protein expression level in hepatic nuclei from C26 and 8025-tumor-bearing mice (Figures S2H–S2O). REV-ERBα expression has diurnal peak close to zeitgeber time (ZT) 9, the time point at which samples were collected from the study animals.

To further explore the potential role of REV-ERBs in hepatocyte gene regulation during cachexia, we integrated publicly

available RNA-seq data from healthy mice with hepatocyte-specific deficiency of both REV-ERBα and REV-ERBβ²⁹ into our analyses. IMAGE-predicted target genes of the NR1D2/RORC motifs were particularly enriched in GC3 of our RNA-seq data (Figure 3C). In line, we found that genes included in this cluster (GC3) were preferentially induced in mice deficient in hepatic REV-ERBα and REV-ERBβ²⁹ at ZT10 (Figure 3D).

Further analysis revealed that motifs recognized by other core clock members such as D-box binding PAR-domain basic



(legend on next page)

leucine zipper transcription factor (DBP) also displayed changes in differential motif activity during cachexia progression (Figure S2G). We observed repression of *Dbp* with diurnal peak close to ZT9 in cachectic mice (Figure 3E). In contrast, expression of clock transcription factors with opposite diurnal peaks and targets of REV-ERB α such as *Arntl* (encoding BMAL1), *Nfil3* (encoding nuclear factor interleukin-3-regulated) and *Npas2* (encoding neuronal PAS domain protein 2) were induced in cachectic animals at ZT9 (Figure 3E).

Together, these results suggest that REV-ERBs act as molecular breaks on expression of genes in GC3. Decreased expression of these transcription factors may contribute to the activation of GC3 genes during cachexia progression.

Restoring hepatic REV-ERB α expression in C26 tumor-bearing mice ameliorates features of cachexia

As we identified decreased expression of *Nr1d1* as a potential driver of transcriptional changes in hepatocytes, we tested whether overexpression of REV-ERB α could have an impact on CCx development. We injected BALB/c mice with an adeno-associated virus (AAV) expressing REV-ERB α or GFP as control from the hepatocyte-specific thyroxine binding globulin (TBG)-promoter³⁰ and subsequently transplanted C26 cells subcutaneously (Figure 4A). Evaluation of protein expression in livers confirmed increased REV-ERB α expression along with decreased BMAL1 expression in mice that received the AAV to express REV-ERB α (Figures S3A–S3C).

REV-ERB α overexpression reduced body weight loss in C26 tumor-bearing animals (Figures 4B and 4C) and significantly increased weights of the heart, GC muscle, and WAT depots (Figures 4D–4F and S3D). Weights of liver, spleen and tumor samples were similar between the groups (Figures 4G, S3E, and S3F). Given the role of systemic inflammation in cachexia,⁶ we next examined whether hepatic REV-ERB α overexpression affected related inflammatory mediators. Circulating levels of key inflammatory cachexia mediators, including IL-6, TNF- α , IL-1 β , and IL-22 were comparable between control and REV-ERB α overexpressing mice (Figures 4H and S3G–S3I), suggesting that the observed effects of the REV-ERB α overexpression in C26 tumor-bearing mice were independent of overall systemic inflammation. However, IL-27, identified as a potential upstream regulator of the hepatic transcriptional response in CCx (Figure 1G), was significantly increased in tumor-bearing mice upon hepatic overexpression of REV-ERB α (Figure 4I).

As heart weights were increased upon hepatic REV-ERB α overexpression in tumor-bearing mice, we analyzed its transcriptome as a prototypic target tissue contributing to CCx mortality.³¹ This analysis revealed the differential expression of 2,560 genes between two or more conditions, which we subsequently grouped into four distinct heart gene expression clusters (Figure 4J). Notably, in cluster two, which was characterized by upregulation in cachectic control C26 tumor-bearing mice and a markedly reduced response upon REV-ERB α overexpression (Figures 4J and S3J), “positive regulation of catabolic processes” was among the top enriched pathways (Figure 4K). In addition, this cluster contained pathways linked to autophagy and macroautophagy (Figure S3K). Indeed, the expression of numerous genes linked to autophagy were significantly reduced in hearts of C26 tumor-bearing mice with hepatic REV-ERB α overexpression compared with GFP controls, including microtubule associated protein 1 light-chain 3 beta (*Map1lc3b*) and BCL2/adenovirus E1B interacting protein 3 (*Bnip3*) (Figure S3K). We validated the reduced expression of *Map1lc3b* via qPCR and at the protein level, further indicating that induction of hepatic REV-ERB α expression reduced autophagy in the heart along with reduced tissue wasting (Figures 4L, S3L, and S3M). In addition, mRNA levels of atrophy-related transcripts tripartite motif containing 63 (*Trim63*) were reduced in hearts of C26 tumor-bearing animals with hepatic REV-ERB α overexpression. While no changes in *Map1lc3b* mRNA expression were observed in GC muscle, increased GC muscle weights associated with significantly reduced levels in atrophy-related transcripts *Trim63* and F-Box protein 32 (*Fbxo32*) in mice with restored hepatic REV-ERB α expression (Figure 4M).

Together, our data suggest that restoring hepatic REV-ERB α expression can ameliorate cachexia in tumor-bearing mice in various target organs.

Cachexia-induced hepatokines promote catabolic processes

Next, we aimed to identify liver-secreted factors that are regulated by REV-ERB α and potentially mediate tissue wasting in CCx. To this end, we defined a list of 13 top candidates from the genes induced in CCx in hepatocytes from GC3 encoding secreted proteins (Figure 1F), based on consistent induction (8-fold) in both our C26 and 8025 cachexia models (Figure S4A). We analyzed their expression in livers of mice with hepatocyte-specific REV-ERB α / β deficiency²⁹ and identified lipopolysaccharide binding protein (*Lbp*), inter-alpha-trypsin

Figure 4. Restoring liver REV-ERB α expression in C26 tumor-bearing mice ameliorates features of cachexia

(A) Experimental setup: BALB/c mice were injected with AAVs for hepatocyte-specific REV-ERB α or GFP (control) expression and implanted with C26 cells subcutaneously 10 days later.
(B) Body weight development of C26 tumor-bearing mice ($n = 10$ /group, two-way ANOVA with Šidák’s multiple comparisons test).
(C–G) Body weight change (C) and weights of heart (D), gastrocnemius (GC) muscle (E), epididymal white adipose tissue (eWAT, F), and tumors (G, $n = 10$ /group, two-tailed t test for C. Two-tailed t test with Welch correction for D and E; Mann-Whitney test for F).
(H and I) Serum levels of IL-6 (H) and IL-27 (I, $n = 10$ /group, two-tailed t test with Welch correction).
(J) K-means clustering of row-scaled expression of differentially expressed genes ($p_{adj} < 0.05$) in hearts ($n = 4$ –10/group).
(K) Functional enrichment analysis using Gene Ontology (biological process) for the indicated GCs in the heart.
(L and M) Heart (L) and GC muscle (M) mRNA levels determined by qPCR of atrophy-related genes *Trim63*, *Fbxo32*, and *Foxo3* and autophagy-related genes *Map1lc3b* and *Bnip3*. ($n = 8$ –10/group, two-tailed t test with Welch correction for comparisons in L, two-tailed t test with Welch correction for *Trim63* in M, two-tailed t test for *Fbxo32* in M). Error bars indicate standard error of the mean; * $p < 0.05$, ** $p < 0.01$, *** $p < 0.001$.
See also Figure S3.

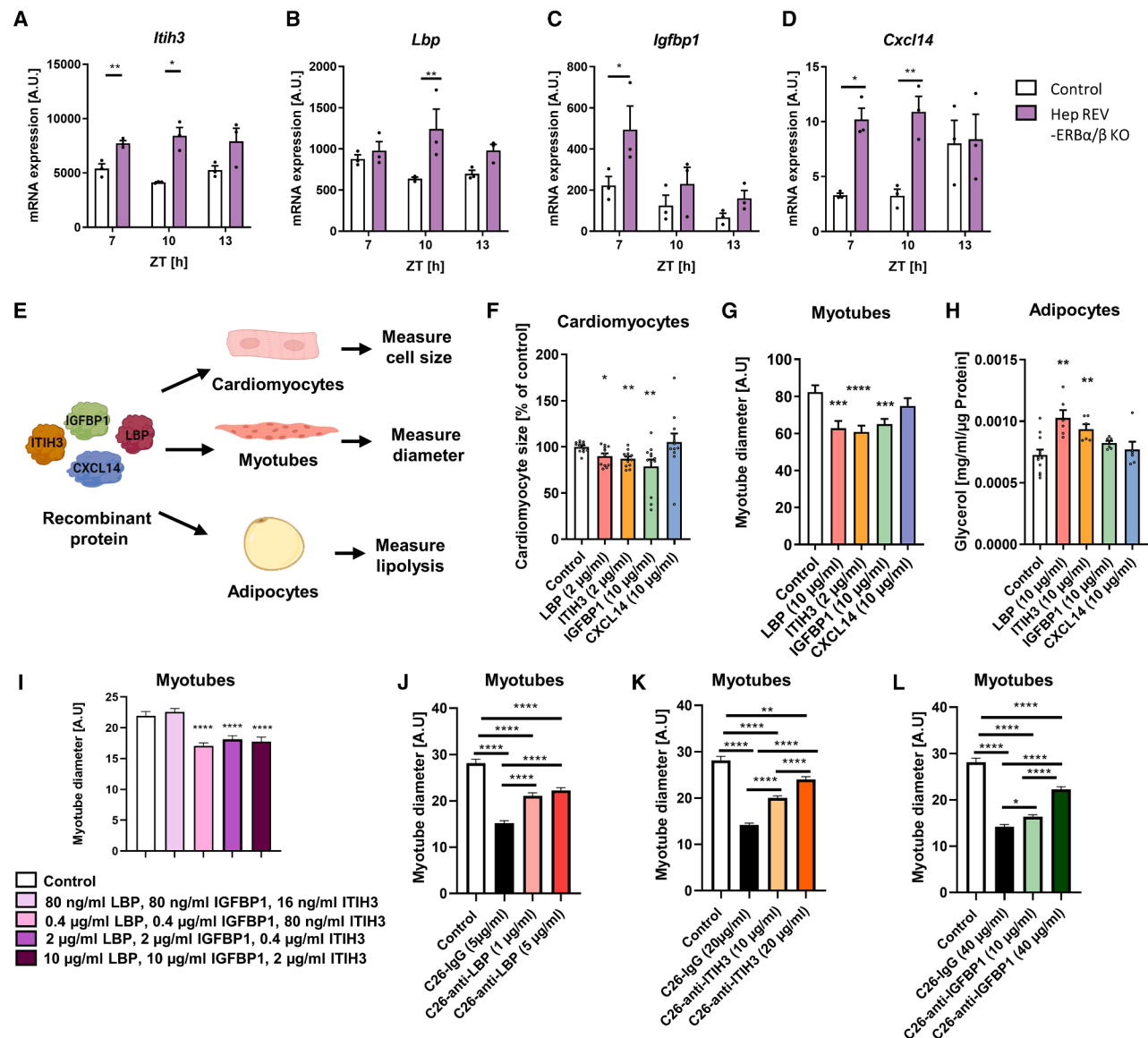


Figure 5. Hepatocyte-secreted factors that are changed upon clock manipulation in cachexia induce catabolic responses *in vitro*

(A–D) Liver mRNA levels of candidate genes in hepatocyte-specific REV-ERB α / β KO mice ($n = 3$, two-way ANOVA, Sidák's multiple comparisons test).

(E) Experimental setup of testing recombinant protein of liver candidates on primary rat cardiomyocytes, C2C12 myotubes and differentiated white adipocytes *in vitro*.

(F) Primary rat cardiomyocytes were treated with the indicated doses of LBP, ITIH3, IGFBP1, or CXCL14 for 24 h and subsequently fixed with paraformaldehyde (PFA). ($n = 12$ /group, two-tailed t test for comparing control vs. LBP and control vs. ITIH3, two-tailed t test with Welch correction for comparing control vs. IGFBP1).

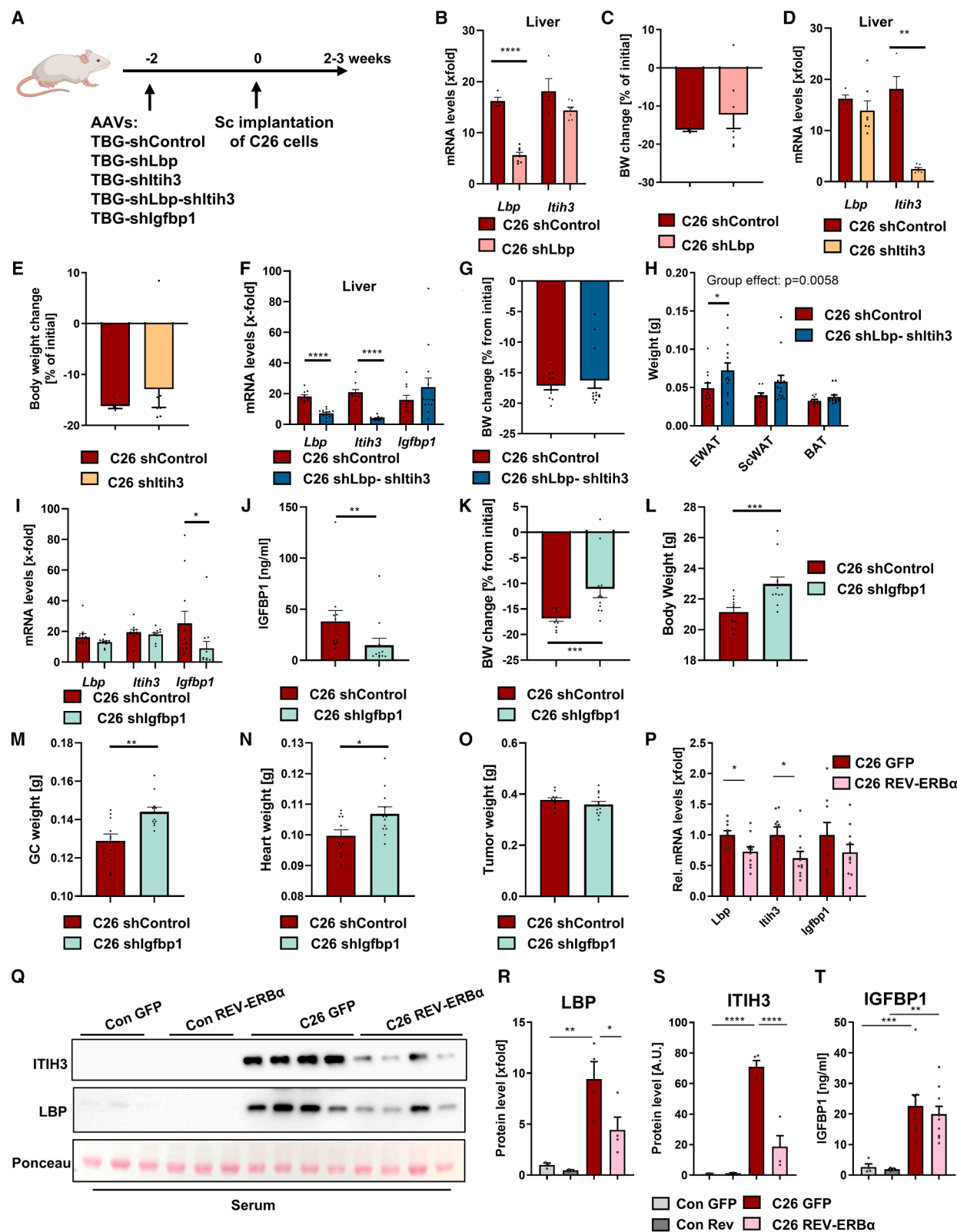
(G) C2C12 myotubes were treated with the indicated doses of LBP, ITIH3, IGFBP1, or CXCL14 for 48 h. Wells were imaged and myotube diameters were measured using ImageJ. Data are representative of three independent experiments. ($n \geq 33$ myotubes per condition, two-tailed t test for comparing control vs. LBP, Mann-Whitney test for control vs. ITIH3 and control vs. IGFBP1).

(H) Differentiated adipocytes were treated with the indicated doses of LBP, ITIH3, IGFBP1, or CXCL14 for 24 h. Glycerol content was measured and normalized to the protein content of each well ($n \geq 6$ per condition, two-tailed t test for comparing control vs. LBP and control vs. ITIH3).

(I) C2C12 myotubes were treated with a combination of the recombinant proteins as indicated for 48 h and myotubes diameters were quantified using ImageJ. Data are representative of two independent experiments. ($n \geq 166$ myotubes per condition, Kruskal-Wallis test with Dunn's multiple comparisons test).

(J–L) C2C12 myotubes were treated with plasma (1%) of C26 tumor-bearing mice in combination with the indicated doses of anti-LBP (J), anti-ITIH3 (K), and anti-IGFBP1 (L) for 48 h or with the respective immunoglobulin G (IgG) isotype control (C26). Cells were fixed with PFA, imaged and the myotube diameters were measured using ImageJ. ($n \geq 125$ myotubes per condition, Kruskal-Wallis test with Dunn's multiple comparisons test). Same values are shown for control group between in (J)–(L). Error bars indicate standard error of the mean; * $p < 0.05$, ** $p < 0.01$, *** $p < 0.001$, **** $p < 0.0001$.

See also Figures S4 and S5.



(legend on next page)

inhibitor heavy-chain H3 (*Itih3*), chemokine (C-X-C motif) ligand 14 (*Cxcl14*) and insulin-like-growth-factor-binding protein 1 (*Igfbp1*) as significantly induced compared with controls at one or more time points analyzed (Figures 5A–5D and S4A). Conversely, we evaluated the expression of these hepatokines in published data from transgenic mice with hepatic REV-ERB α overexpression³² and observed a marked reduction in *Lbp*, *Itih3*, and *Igfbp1* expression during the light phase (Figure S4B). Additionally, evaluation of published liver REV-ERB α chromatin immunoprecipitation (ChIP) data³³ revealed genomic binding of REV-ERB α at *Lbp*, *Igfbp1* and *Itih3* promoters and adjacent regulatory regions (Figures S4C–S4E). These data support a role of REV-ERB α as a transcriptional repressor for these hepatokines. By contrast, *Cxcl14* did not appear to be tightly linked to REV-ERB α genomic binding (Figure S4F).

Next, we assessed candidate hepatokine expression in mice with hepatic BMAL1 deficiency.³⁴ As expected, reduced hepatic *Arntl* (encoding BMAL1) expression resulted in *Nr1d1* (encoding REV-ERB α) downregulation in the liver (Figures S4G and S4H). Notably, hepatokine levels were elevated at both the mRNA level and in circulation in BMAL1-deficient mice (Figures S4I–S4O), mirroring the pattern observed under REV-ERB α knockdown. Collectively, these data suggest that activation of our identified hepatokines is a result of REV-ERB α deficiency. Additionally, we observed a similar reduction in liver *Nr1d1* mRNA levels and an increase in *Lbp*, *Itih3*, and *Igfbp1* levels in two additional CCx models: the Lewis lung carcinoma (LLC) model (Figures S4P–S4T), in which LLC cells were transplanted subcutaneously, and the Apc^{Min/+} model (Figures S4U–S4Y), a genetic model of colorectal cancer.^{35,36} These findings indicate that the downregulation of REV-ERB α and the associated increase in hepatokine secretion may be a common feature of CCx across different models.

To test whether the identified liver-secreted factors can elicit catabolic responses in cell types affected by cachexia, we treated primary rat cardiomyocytes, C2C12 myotubes, and differentiated white adipocytes with recombinant protein *in vitro* (Figure 5E).

In primary rat cardiomyocytes and C2C12 myotubes, recombinant LBP, ITIH3, and IGFBP1 induced a significant and dose-dependent decrease in cardiomyocyte cell size (Figures 5F and S5A–S5E) and myotube diameter (Figures 5G and S5F–S5J), indicating an atrophic effect. No changes were observed after treatment with recombinant CXCL14 (Figures 5F, 5G, S5D, and S5I). In differentiated white adipocytes, recombinant LBP and ITIH3 treatments led to an increase in glycerol release in the media indicating an induction of lipolysis in adipocytes (Figures 5H, S5K, and S5L). In contrast, IGFBP1 and CXCL14 treatment did not lead to a significant increase in media glycerol levels (Figures 5H, S5M, and S5N). Combining LBP, ITIH3, and IGFBP1 treatment led to an atrophic effect even at lower concentrations in C2C12 myotubes (Figure 5I). Treatment of C2C12 myotubes with plasma from C26 tumor-bearing mice also induced atrophy, an effect that was abrogated by pretreatment of the plasma with neutralizing antibodies against the hepatokines, highlighting their therapeutic potential (Figures 5J–5L and S5O).

To assess the contribution of hepatokines to CCx *in vivo*, we performed hepatic AAV-mediated short hairpin RNA (shRNA) knockdowns of *Lbp* (shLbp), *Itih3* (shItih3), and *Igfbp1* (shIgfbp1), either individually or pairwise combinations in the C26 cachexia model (Figure 6A). An individual knockdown of *Lbp* and *Itih3* reduced their respective mRNA levels in the liver of C26 tumor-bearing mice, but it did not alter body weight loss or affect tissue weights compared with control AAVs (shControl) (Figure 6B–6E, S6A–S6F, and S6H–S6M). While no improvements in muscle function were observed upon *Itih3* knockdown, the *Lbp* knockdown associated with increased

Figure 6. Knockdown of hepatokines ameliorates features of cancer cachexia *in vivo*

- (A) BALB/c mice were injected with AAVs encoding shRNAs under the control of the hepatocyte-specific TBG promoter to knock down either *Lbp* (shLbp), *Itih3* (shItih3), *Lbp*, and *Itih3* (shLbp-shItih3) together or *Igfbp1* (shIgfbp1). Control mice received a scrambled control shRNA (shControl). Mice were implanted with C26 cells subcutaneously 2 weeks later.
- (B) Liver mRNA expression of *Lbp* and *Itih3* upon *Lbp* knockdown in C26 tumor-bearing mice ($n = 4$ –7/group, two-tailed t test for group-wise comparison of *Lbp* expression).
- (C) Changes in body weight ($n = 4$ –7/group).
- (D) Liver mRNA expression of *Lbp* and *Itih3* upon *Itih3* knockdown in C26 tumor-bearing mice ($n = 4$ –7/group, two-tailed t test for group-wise comparison of *Itih3* expression). Values of control animals are the same as in (B).
- (E) Changes in bodyweight upon *Itih3* knockdown in C26 tumor-bearing mice ($n = 4$ –7/group). Values of control animals are the same as in (C).
- (F) Liver mRNA expression of hepatokines upon combined *Lbp* and *Itih3* knockdown in C26 tumor-bearing mice ($n = 11$ –14/group, group-wise comparison: two-tailed t test for *Lbp* expression, Mann-Whitney test for *Itih3* expression).
- (G) Changes in body weight ($n = 11$ –14/group).
- (H) Adipose tissues weights ($n = 11$ –14/group, two-way ANOVA, Šidák's multiple comparisons test).
- (I) Liver mRNA expression of hepatokines upon *Igfbp1* knockdown in C26 tumor-bearing mice ($n = 11$ –12/group, Mann-Whitney test for group-wise comparison of *Igfbp1* expression).
- (J) Circulating levels of IGFBP1 were determined by ELISA ($n = 11$ –14/group, Mann-Whitney test).
- (K) Changes in body weight of C26 tumor-bearing mice upon *Igfbp1* knockdown ($n = 11$ –12/group, Mann-Whitney test).
- (L–O) Final body (L) or tissue (M–O) weights upon *Igfbp1* knockdown ($n = 11$ –12/group, Mann-Whitney test for L, two-tailed t test for M and N).
- (P) Liver mRNA levels of candidate genes in C26 tumor-bearing control mice (C26 GFP) or upon REV-ERB α restoration (C26 REV-ERB α) ($n = 9$ –10/group, two-tailed t test for pairwise comparison of gene expression).
- (Q–S) Protein expression of ITIH3 and LBP in serum (Q) and subsequent quantification (R and S) ($n = 3$ –4/group, ANOVA, Šidák's multiple comparisons test).
- (T) Serum IGFBP1 levels of C26 tumor-bearing mice were determined via ELISA ($n = 4$ –10/group, ANOVA, Šidák's multiple comparisons test). Error bars indicate standard error of the mean; * $p < 0.05$, ** $p < 0.01$, *** $p < 0.001$, **** $p < 0.001$.

See also Figure S6.

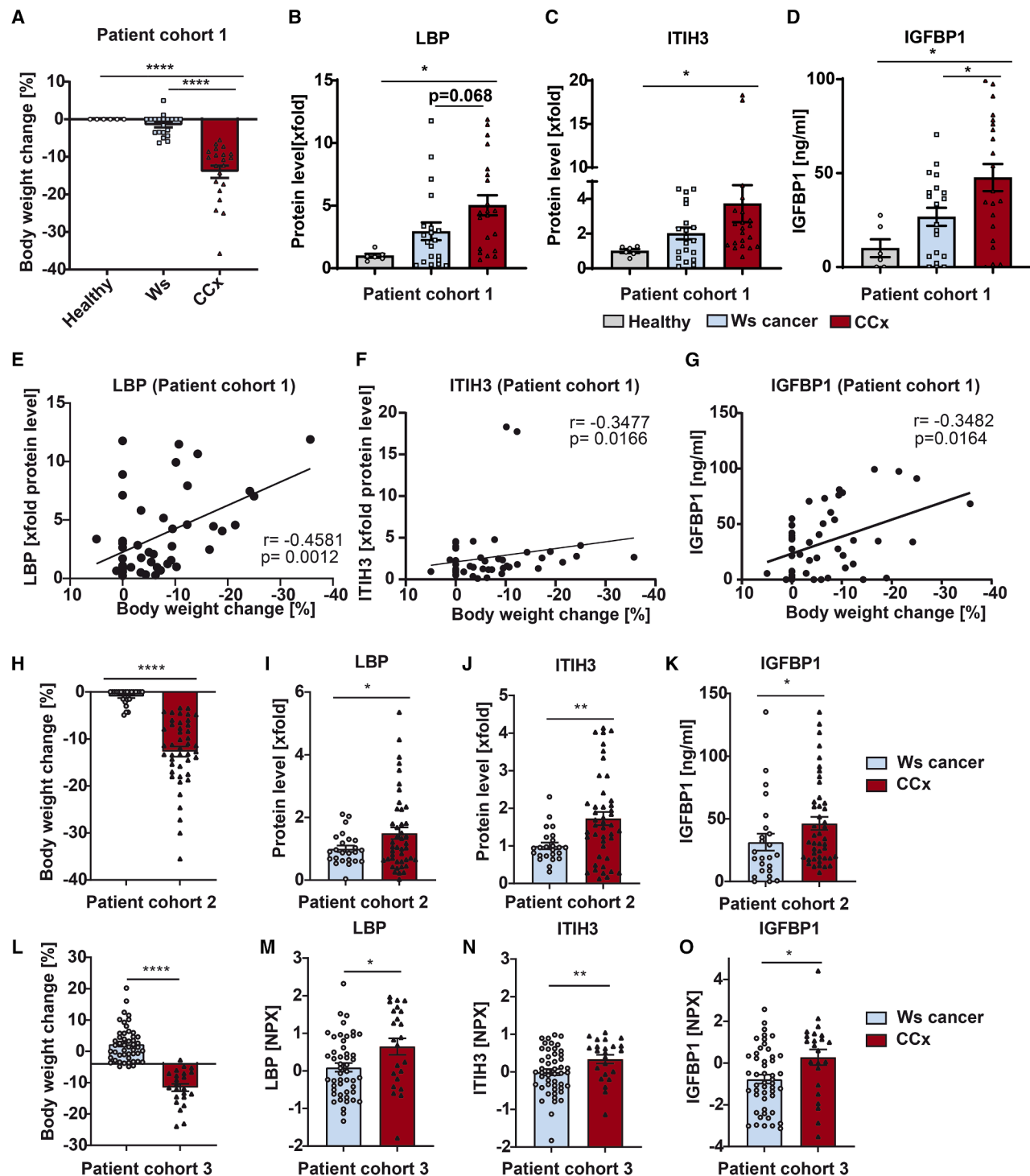


Figure 7. Hepatocyte-secreted factors are increased in cachectic cancer patients

(A) Relative body weight change in a cohort of healthy humans ($n = 6$), weight-stable (ws, $n = 20$), and cachectic gastrointestinal cancer ($n = 21$) patients (patient cohort 1, Kruskal-Wallis test with Dunn's multiple comparisons test).

(B and C) Quantification of circulating protein levels of LBP (B) and ITIH3 (C) in patient cohort 1 were determined by western blot (Kruskal-Wallis test with Dunn's multiple comparisons test).

(D) Circulating levels of IGFBP1 in of individuals of patient cohort 1 were determined by ELISA (ANOVA, Tukey's multiple comparisons test).

(E–G) Correlation (Spearman) of circulating levels of LBP (E), ITIH3 (F), and IGFBP1 (G) with changes in body weight of patient cohort 1.

(legend continued on next page)

grip strength indicating improved muscle function (Figures S6G and S6N).

A combined knockdown of *Lbp* and *Itih3* (shLbp-Itih3) was confirmed by a reduction in liver mRNA expression, which resulted in significantly lower plasma protein levels (Figures 6F and S6O–S6Q) suggesting hepatocytes as a major source of these factors in the circulation in CCx. The combined knockdown led to an increase in eWAT weight, suggesting a protective effect against adipose tissue loss in C26 tumor-bearing mice (Figures 6HS6). However, overall body weight, GC muscle, heart, liver, and tumor weights were not affected (Figures 6G and S6R–S6V). In addition, we observed a trend to improve muscle function (Figure S6W).

Knockdown of *Igfbp1* was confirmed by a marked reduction in liver *Igfbp1* mRNA levels (Figure 6I), which also translated to significantly lower circulating IGFBP1 levels (Figure 6J), while not affecting plasma LBP and ITIH3 levels (Figures S6X–S6Z). Notably, hepatic *Igfbp1* knockdown led to an amelioration of body weight loss in C26 tumor-bearing mice (Figures 6K and 6L). In addition, hepatic IGFBP1 knockdown improved GC muscle weight, heart weights, and muscle function, whereas adipose tissue depots, liver, and tumor weights remained unchanged compared with C26 tumor-bearing mice treated with control AAV (Figures 6M–6O and S6AA–S6AC).

Confirming the critical role of these hepatokines, we observed a significant reduction of *Lbp* and *Itih3* in livers of tumor-bearing mice with restored REV-ERB α (Figure 6P). Similarly, circulating levels of LBP and ITIH3 were markedly induced in C26 tumor-bearing mice and again reduced upon REV-ERB α overexpression (Figures 6Q–6S). IGFBP1 levels were similar in cachectic C26 tumor-bearing mice with hepatic REV-ERB α overexpression and GFP controls at the protein and mRNA level (Figures 6P and 6T).

In summary, we identified REV-ERB α -regulated hepatokines that are elevated in circulation during CCx and capable of inducing catabolic processes in target cells *in vitro*. Hepatic knockdown of these hepatokines altered features of CCx *in vivo*, with IGFBP1 emerging as a key driver of systemic muscle wasting. These findings underscore the liver's role in promoting tissue wasting in CCx through the secretion of cachexia-induced hepatokines.

Liver-secreted factors are increased in cachectic cancer patients

Finally, we evaluated whether the liver-secreted factors we identified were also increased in cachectic patients with different cancer types. The first cohort consisted of patients with different gastrointestinal cancer entities (patient cohort 1) that were either weight stable or cachectic, alongside healthy controls (Table S1). Cachectic cancer patients displayed an average

change in body weight of -13.95% compared with a change of -1.52% in weight-stable cancer patients (Figure 7A). In addition, cachectic cancer patients displayed higher circulating levels of C-reactive protein and lower levels of hemoglobin, albumin, and glucose (Table S1).²² In agreement with the mouse data, plasma levels of LBP, ITIH3, and IGFBP1 were significantly increased in cachectic cancer patients compared with healthy controls (Figures 7B, 7C, and S7A). In addition, IGFBP1 was significantly increased in cachectic cancer patients compared with weight-stable cancer patients (Figure 7D). Of note, the circulating plasma levels of LBP, ITIH3, and IGFBP1 showed a significant correlation with the average change in body weight reported for the human subjects (Figures 7E–7G). Patient cohort 2 included 24 weight-stable and 44 cachectic patients with pancreatic cancer (Figure 7H; Table S2). Consistent with previous findings, circulating levels of LBP, ITIH3, and IGFBP1 were elevated in cachectic patients compared with their weight-stable counterparts (Figures 7I–7K and S7B). Moreover, LBP and ITIH3 levels correlated significantly with body weight loss (Figures S7C–S7E). Finally, we evaluated hepatokine levels in 72 lung cancer patients, subdivided into 49 weight-stable and 23 cachectic individuals (patient cohort 3; Figure 7L; Table S3). Here, plasma samples were analyzed using a targeted proteomics approach. Similar to patient cohorts 1 and 2, LBP, ITIH3, and IGFBP1 protein expression were significantly increased compared with weight-stable cancer patients (Figures 7M–7O) and LBP and ITIH3 levels correlated significantly with body weight loss (Figures S7F and S7G).

In conclusion, our findings demonstrate that the hepatokines identified in our CCx models are consistently elevated in cachectic cancer patients across different tumor types, highlighting the translational values of our findings.

DISCUSSION

In this study, we performed comprehensive, multilayered analyses of hepatic responses under systemic wasting conditions. We uncovered a distinct cachexia-induced gene program that distinguishes cachectic from weight-stable cancer across various models. Our integrative analysis identified that the marked downregulation of REV-ERB α contributes to hepatic transcriptional reprogramming in CCx, revealing circadian clock components as key regulators. Restoring REV-ERB α expression in the liver reduced cancer-induced weight loss in C26 tumor-bearing mice. We found increased levels of REV-ERB α -regulated hepatokines in circulation during CCx, which induced catabolic processes *in vitro*. Hepatocyte-specific knockdown of these hepatokines, most prominently IGFBP1, ameliorated features of CCx *in vivo*. Notably,

(H) Relative body weight change in a cohort of weight-stable (ws, $n = 24$) and cachectic pancreatic cancer ($n = 44$) patients (patient cohort 2, Mann-Whitney test).

(I and J) Quantification of circulating protein levels evaluated by western blot of LBP (I, two-tailed t test with Welch correction) and ITIH3 (J, Mann-Whitney test) in patient cohort 2.

(K) Circulating levels of IGFBP1 of patient cohort 2 were determined by ELISA (Mann-Whitney test).

(L) Relative body weight change in a cohort of weight-stable (ws, $n = 49$) and cachectic lung cancer ($n = 23$) patients (Patient cohort 3, Mann-Whitney test).

(M–O) Normalized protein expression (NPX) of LBP (M), ITIH3 (N), and IGFBP1 (O) in plasma analyzed via a targeted proteomics approach (two-tailed t test). Error bars indicate standard error of the mean; * $p < 0.05$, ** $p < 0.01$, **** $p < 0.0001$. WSC/Ws, weight-stable; CCx, cancer cachexia.

See also Figure S7.

these protein factors are also associated with CCx in human patients.

Previous studies linked CCx with changes in liver function, exemplified by an impaired capacity for oxidative phosphorylation in mitochondria,³⁷ dysfunction of hepatic lipid metabolism^{38,39} and inflammation-induced cholestasis.¹⁵ While the involvements of these functional alterations to directly drive tissue wasting in CCx remains unclear, we provide evidence that hepatocyte-secreted factors promote tissue wasting in other parts of the body.

Transcriptomic profiling revealed a hepatic gene expression signature specific to cachectic, but not weight-stable, cancer. This included genes associated with acute-phase proteins such as fibrinogen (*Fga*, *Fgb*, and *Fga*) and serum-amyloid A (*Saa1* and *Saa2*), consistent with acute-phase response activation in CCx.¹¹ While our study focused on hepatocytes, the role of other liver cell types in CCx onset and progression warrants further investigation.

Fitting a general pro-inflammatory state of the liver in CCx,⁸ our transcriptomic profiling identified STAT3 and GR as additional drivers of transcriptional changes occurring in CCx. Their increased activity might be a result of activation by inflammatory factors—produced by the tumor and the host—that are usually increased in cachexia, such as IL-6 and glucocorticoids.^{8,40} In accordance, our NicheNet analysis predicted IL-6 as upstream modulator of transcriptional changes in CCx and both GR and STAT3 have been shown to mediate inflammatory responses in CCx in other tissues.^{41–43}

Most notably, our analysis identified components of the circadian clock in hepatocytes as key modulators of cachexia-induced transcriptional reprogramming. Circadian regulation of gene expression is of great importance for maintaining liver physiology and disturbances of the liver clock are linked to metabolic diseases.⁴⁴ Our data revealed the downregulation of *Nr1d1* as a hallmark of the cachectic response in hepatocytes suggesting potential disturbances of the circadian clock.

In contrast to the well-characterized activators of STAT3 and GR, the upstream regulators responsible for the disruption REV-ERB α expression in our CCx models remain to be identified. Interestingly, the GR is known to repress *Nr1d1* mRNA expression by interacting with the CLOCK complex.⁴⁵ This suggests that the GR may play an upstream regulatory role in controlling *Nr1d1* (encoding REV-ERB α) expression in CCx, and these potential relationships warrant further exploration.

Contrary to our data, hepatic gene expression of *Nr1d1* and *Arntl1* was unaffected at the mRNA level in a lung adenocarcinoma model that is associated with body weight loss.^{46,47} However, while the involvement of the clock for the development of the cachectic phenotype was not assessed in these publications, it was shown that REV-ERB α protein was destabilized by a protein-kinase-A-dependent mechanism in their model.⁴⁶ It is worth considering whether the stability of REV-ERB α protein is also influenced in the CCx models we employed. However, given that *Nr1d1* (encoding REV-ERB α) mRNA expression is downregulated in our CCx models, REV-ERB α protein stability appears less important in our models.

By restoring REV-ERB α expression in hepatocytes of C26 tumor-bearing mice, we were able to ameliorate tissue wasting without altering circulating levels of key inflammatory mediators of cachexia, including IL-6. Interestingly, REV-ERB α overexpression led to an increase in circulating IL-27, a multifunctional cytokine with both pro- and anti-inflammatory roles.⁴⁸

Whether this elevation in IL-27 serves as a compensatory mechanism to reinforce cachectic signaling or contributes to the mitigation of tissue wasting remains an open question for future investigation.

Mechanistically, we identified LBP, ITIH3, and IGFBP1 as liver-secreted factors that are regulated by REV-ERB α . While IGFBP1 levels only tended to be lower upon REV-ERB α restoration in C26 tumor-bearing mice, its expression was induced upon REV-ERB α deficiency, suggesting a repressive effect of REV-ERB α on *Igfbp1* expression. We speculate different kinetics and/or the specific time point chosen for analysis may account for similar *Igfbp1* expression levels upon REV-ERB α overexpression in CCx. In addition, other transcription factors, such as the GR, which is known to induce *Igfbp1* mRNA expression, may contribute to the induction of *Igfbp1* expression in CCx.⁴⁹ Importantly, we show that LBP, ITIH3, and IGFBP1 were able to elicit catabolic processes in cardiomyocytes, myotubes, and/or adipocytes. In addition, antibody treatment against the hepatokines partially rescued myotube atrophy *in vitro*, which further supports their roles as hepatic cachexia mediators. Notably, hepatocyte-specific knockdown of *Lbp* and *Itih3* together mitigated white fat loss in C26 tumor-bearing mice, while hepatic knockdown of *Igfbp1* significantly ameliorated body weight loss, suggesting a dominant role for IGFBP1 in systemic muscle wasting. IGFBPs regulate the bioavailability of insulin-like growth factor 1 (IGF-1), a key anabolic factor essential for maintaining muscle mass,⁵⁰ suggesting that the pronounced increase in circulating IGFBP1 in CCx reduces IGF-1 activity, exacerbating muscle loss. This aligns with a study in *Drosophila* that showed ImpL2, a secreted protein functionally similar to IGFBP7, drives systemic organ wasting.⁵¹

In human cancer patients, the hepatokines LBP, ITIH3, and IGFBP1 were increased in plasma of cachectic gastrointestinal, pancreatic, and lung cancer cases, indicating that our findings from mouse models translate to CCx in humans. In line with our data, increased LBP serum levels have been reported for CCx in mice and humans previously and might be linked to increased gut permeability in CCx.^{52,53}

Collectively, we identified the circadian clock component REV-ERB α as a key regulator of transcriptional reprogramming in CCx and show that by modulating the expression of this circadian repressor can improve the outcome of CCx. Thereby, our data indicate that the liver can promote cachexia progression via systemic tissue crosstalk. We provide evidence for REV-ERB α -regulated factors that elicit catabolic responses in other cell types and show that these factors strongly correlate with cachexia in human cancer patients. Thus, our study identifies circadian clock components in the liver as a potential target to ameliorate CCx.

Limitations of the study

Our preclinical experiments were conducted exclusively in male mice, not accounting for potential sex differences in our findings. However, increased levels of the identified hepatokines contributing to systemic wasting in cachexia were confirmed in samples

from both male and female weight-stable and cachectic patients. While the observed changes in expression of specific circadian clock transcription factors in mice suggest a disruption of the hepatocyte clock in cachexia, we did not assess this disruption in the context of altered periodicity. To formally demonstrate such changes, tissue sampling from cachectic and control animals across the circadian cycle will be necessary. Additionally, although expressing REV-ERB α under the control of the TBG promoter ameliorated disease progression, restoration of gene expression periodicity likely requires further studies to identify intervention points upstream of blunted REV-ERB α expression in cachexia.

RESOURCE AVAILABILITY

Lead contact

Requests for further information and resources should be directed to and will be fulfilled by the lead contact, Mauricio Berriel Diaz (mauricio.berrieldiaz@helmholtz-munich.de).

Materials availability

New reagents and materials generated in this study are listed in the [key resources table](#) and will be made available on request, but we may require a completed materials transfer agreement if there is potential for commercial application.

Data and code availability

Sequencing data will be publicly available as of the date of publication and are deposited at GEO under the accession numbers: GEO: GSE293096 (liver RNA-seq), GEO: GSE293099 (liver ATAC-seq), and GEO: GSE293093 (heart RNA-seq). Original code is available at Zenodo as of the date of publication. The DOI is listed in the [key resources table](#).

Any additional information required to reanalyze the data reported in this paper is available from the [lead contact](#) upon request.

ACKNOWLEDGMENTS

We thank Lisa Mehr, Daniela Haß, Raúl Terrón Expósito, Alexandra Grüttner, Kerstin Lohr, Nadine Rink, and Adriano Maida from the Institute for Diabetes and Cancer (IDC, Helmholtz Munich) for excellent technical and operational support. We thank Rudolf Zechner and Martina Schweiger from the Institute of Molecular Biosciences (University of Graz) for kindly providing NC26 cancer cell lines with permission of Graham Robertson from ANZAC Research Institute (University of Sydney). We thank James M. Wilson and Mitchell Lazar from University of Pennsylvania for the pAAV-GFP and pAAV-REV-ERB α plasmids, respectively. We thank Ronald Evans (Salk Institute for Biological Sciences) for sharing the REV-ERB α antibody produced in the Evans lab. We thank Siegfried Ussar from the Institute for Diabetes and Obesity (Helmholtz Munich) for providing the SV40 large T-antigen for adipocyte immortalization. [Figures 1A, 4A, 5E, 6A](#), and the graphical abstract were generated with [BioRender.com](#). This work was supported by the European Research Council (ERC) under the European Union's Horizon 2020 research and innovation program (#949017) to M.R. and a grant from the Else Kröner-Fresenius-Stiftung (2020 EKSE.23) to S.H., as well as the Edith-Haberland-Wagner Stiftung. D. K. received support by an Erwin Schrödinger Fellowship from the Austrian Science Fund (FWF, J4224-B34). The work was also financially supported by grants from the Danish National Research Foundation (DNRF grant no. 141 to ATLAS) and the Novo Nordisk Foundation (NNFOC150019050) to S.F.S. A.L. was supported by a fellowship from the Novo Nordisk Foundation (NNF16OC0020742). A.E. received funding by the Deutsche Forschungsgemeinschaft (DFG) under Germany's Excellence Strategy (EXC 2145 SyNergy, grant 390857198). J.B. was funded by the CRC1550 (project ID 464424253) and DZHK (BMBF). O.P. was supported by a Clinical Leave Stipend from the German Center for Infection Research (Deutsches Zentrum für Infektionsforschung [DZIF], grant T107.001). The TRACERx study (ClinicalTrials.gov:

NCT01888601) is sponsored by University College London (UCL/12/0279) and has been approved by an independent Research Ethics Committee (13/LO/1546). TRACERx is funded by Cancer Research UK (C11496/A17786) and is coordinated through the Cancer Research UK and UCL Cancer Trials Centre, which has a core grant from CRUK (C444/A15953). We thank the patients and relatives who participated in the TRACERx study and all site personnel, investigators, funders, and industry partners who supported the generation of the data within this study. R.S. and M.J.-H. are funded by the CANCAN Cancer Grand Challenges partnership funded by Cancer Research UK (CGCATF-2021/100035) and the NIH National Cancer Institute (OT2CA278701-01S2). K.H. is funded by Cancer Research UK. M.J.-H. is a CRUK Career Establishment Awardee and has received funding from Cancer Research UK, NIH National Cancer Institute, IASLC International Lung Cancer Foundation, Lung Cancer Research Foundation, Rosetrees Trust, UKI NETs, and NIHR University College London Hospitals Biomedical Research Centre.

AUTHOR CONTRIBUTIONS

D.K., S.F.S., A.L., J.M., K.B.S., and C.-E.M. conducted experiments and analyzed, integrated, and interpreted data. S.F.S. and P.W. analyzed sequencing data. D.K., S.F.S., and M.B.D. conceptualized, managed, and coordinated the project. K.A.D. evaluated REV-ERB α overexpression and ChIP-seq data. P.M., J.G., P.B., K.K.C., N.S., M.H.d.A., M.R., and J.B. supported *in vivo* and/or *in vitro* experiments. J.B. and K.B.S. led cardiomyocyte experiments. E.S., J.P.O., J.D.C.C.L., M.S., M.E.M., and O.P. provided human plasma samples. R.S., K.H., C.S., and M.J.-H. provided data on human lung cancer patients. A.J.A., M.E., A.E., and K.A.D. provided critical input and edited the manuscript. D.K. and S.F.S. wrote the manuscript. D.K. revised the manuscript. M.B.D. and S.H. supervised the study, interpreted data, and edited the manuscript.

DECLARATION OF INTERESTS

S.H. serves on the scientific advisory board of Actimed Therapeutics Ltd (UK). M.J.-H. has consulted for Astex Pharmaceuticals, Pfizer, and Achilles Therapeutics; is a member of the Achilles Therapeutics Scientific Advisory Board and Steering Committee; and has received speaker honoraria from Pfizer, Astex Pharmaceuticals, Oslo Cancer Cluster, Bristol Myers Squibb, and Genentech.

STAR★METHODS

Detailed methods are provided in the online version of this paper and include the following:

- [KEY RESOURCES TABLE](#)
- [EXPERIMENTAL MODEL AND STUDY PARTICIPANT DETAILS](#)
 - Animal models
 - Patient cohorts and samples
- [METHOD DETAILS](#)
 - Cell culture
 - Generation of adeno associated virus (AAV)
 - Isolation of GFP-tagged nuclei
 - Tissue RNA isolation and quantitative PCR
 - RNA-seq from nuclei: isolation to sequencing
 - ATAC-seq library construction and sequencing
 - Western Blot
 - ELISA
 - Myotube treatment and diameter analysis
 - Cardiomyocyte treatment and size quantification
 - Adipocyte treatment and glycerol measurement
 - Neutralizing antibody treatment of myotubes
- [QUANTIFICATION AND STATISTICAL ANALYSIS](#)
 - Processing and analyses of RNA-seq data
 - Analyses of public RNA-seq data
 - Pathway analysis
 - Upstream Regulator Analysis
 - Processing and analyses of ATAC-seq data

- Transcription factor motif activity and targets
- Statistics

SUPPLEMENTAL INFORMATION

Supplemental information can be found online at <https://doi.org/10.1016/j.cell.2025.06.039>.

Received: December 5, 2023

Revised: March 26, 2025

Accepted: June 25, 2025

REFERENCES

1. Argilés, J.M., Busquets, S., Stemmler, B., and López-Soriano, F.J. (2014). Cancer cachexia: understanding the molecular basis. *Nat. Rev. Cancer* 14, 754–762. <https://doi.org/10.1038/nrc3829>.
2. von Haehling, S., Anker, M.S., and Anker, S.D. (2016). Prevalence and clinical impact of cachexia in chronic illness in Europe, USA, and Japan: facts and numbers update 2016. *J. Cachexia Sarcopenia Muscle* 7, 507–509. <https://doi.org/10.1002/jcsm.12167>.
3. Baracos, V.E., Martin, L., Korc, M., Guttridge, D.C., and Fearon, K.C.H. (2018). Cancer-associated cachexia. *Nat. Rev. Dis. Primers* 4, 17105. <https://doi.org/10.1038/nrdp.2017.105>.
4. Porporato, P.E. (2016). Understanding cachexia as a cancer metabolism syndrome. *Oncogenesis* 5, e200. <https://doi.org/10.1038/oncsis.2016.3>.
5. Fearon, K.C.H., Glass, D.J., and Guttridge, D.C. (2012). Cancer cachexia: mediators, signaling, and metabolic pathways. *Cell Metab.* 16, 153–166. <https://doi.org/10.1016/j.cmet.2012.06.011>.
6. Berriel Diaz, M., Rohm, M., and Herzig, S. (2024). Cancer cachexia: multi-level metabolic dysfunction. *Nat. Metab.* 6, 2222–2245. <https://doi.org/10.1038/s42255-024-01167-9>.
7. Schmidt, S.F., Rohm, M., Herzig, S., and Berriel Diaz, M. (2018). Cancer Cachexia: More Than Skeletal Muscle Wasting. *Trends Cancer* 4, 849–860. <https://doi.org/10.1016/j.trecan.2018.10.001>.
8. Argilés, J.M., Stemmler, B., López-Soriano, F.J., and Busquets, S. (2018). Inter-tissue communication in cancer cachexia. *Nat. Rev. Endocrinol.* 15, 9–20. <https://doi.org/10.1038/s41574-018-0123-0>.
9. Falconer, J.S., Fearon, K.C., Ross, J.A., Elton, R., Wigmore, S.J., Garden, O.J., and Carter, D.C. (1995). Acute-phase protein response and survival duration of patients with pancreatic cancer. *Cancer* 75, 2077–2082. [https://doi.org/10.1002/1097-0142\(19950415\)75:8<2077::aid-cnrc2820750808>3.0.co;2-9](https://doi.org/10.1002/1097-0142(19950415)75:8<2077::aid-cnrc2820750808>3.0.co;2-9).
10. Fearon, K.C., Barber, M.D., Falconer, J.S., McMillan, D.C., Ross, J.A., and Preston, T. (1999). Pancreatic cancer as a model: inflammatory mediators, acute-phase response, and cancer cachexia. *World J. Surg.* 23, 584–588. <https://doi.org/10.1007/pl00012351>.
11. Rohm, M., Zeigerer, A., Machado, J., and Herzig, S. (2019). Energy metabolism in cachexia. *EMBO Rep.* 20, e47258. <https://doi.org/10.15252/embr.201847258>.
12. Narsale, A.A., Enos, R.T., Puppa, M.J., Chatterjee, S., Murphy, E.A., Fayad, R., Pena, M.O., Durstine, J.L., and Carson, J.A. (2015). Liver inflammation and metabolic signaling in ApcMin/+ mice: the role of cachexia progression. *PLoS One* 10, e0119888. <https://doi.org/10.1371/journal.pone.0119888>.
13. Narsale, A.A., Puppa, M.J., Hardee, J.P., VanderVeen, B.N., Enos, R.T., Murphy, E.A., and Carson, J.A. (2016). Short-term pyrrolidine dithiocarbamate administration attenuates cachexia-induced alterations to muscle and liver in ApcMin/+ mice. *Oncotarget* 7, 59482–59502. <https://doi.org/10.18632/oncotarget.10699>.
14. Rosa-Caldwell, M.E., Brown, J.L., Lee, D.E., Wiggs, M.P., Perry, R.A., Haynie, W.S., Caldwell, A.R., Washington, T.A., Lo, W.J., and Greene, N.P. (2020). Hepatic alterations during the development and progression of cancer cachexia. *Appl. Physiol. Nutr. Metab.* 45, 500–512. <https://doi.org/10.1139/apnm-2019-0407>.
15. Thibaut, M.M., Sboarina, M., Roumain, M., Potgens, S.A., Neyrinck, A.M., Destree, F., Gillard, J., Leclercq, I.A., Dachy, G., Demoulin, J.B., et al. (2021). Inflammation-induced cholestasis in cancer cachexia. *J. Cachexia Sarcopenia Muscle* 12, 70–90. <https://doi.org/10.1002/jcsm.12652>.
16. Ferrer, M., Mourikis, N., Davidson, E.E., Kleeman, S.O., Zaccaria, M., Habel, J., Rubino, R., Gao, Q., Flint, T.R., Young, L., et al. (2023). Ketogenic diet promotes tumor ferroptosis but induces relative corticosterone deficiency that accelerates cachexia. *Cell Metab.* 35, 1147–1162.e7. <https://doi.org/10.1016/j.cmet.2023.05.008>.
17. Goncalves, M.D., Hwang, S.K., Pauli, C., Murphy, C.J., Cheng, Z., Hopkins, B.D., Wu, D., Loughran, R.M., Emerling, B.M., Zhang, G., et al. (2018). Fenofibrate prevents skeletal muscle loss in mice with lung cancer. *Proc. Natl. Acad. Sci. USA* 115, E743–E752. <https://doi.org/10.1073/pnas.1714703115>.
18. Loft, A., Herzig, S., and Schmidt, S.F. (2021). Purification of GFP-tagged nuclei from frozen livers of INTACT mice for RNA- and ATAC-sequencing. *Star Protoc.* 2, 100805. <https://doi.org/10.1016/j.xpro.2021.100805>.
19. Deal, R.B., and Henikoff, S. (2010). A simple method for gene expression and chromatin profiling of individual cell types within a tissue. *Dev. Cell* 18, 1030–1040. <https://doi.org/10.1016/j.devcel.2010.05.013>.
20. Kaltenecker, D., Al-Maskari, R., Negwer, M., Hoeher, L., Kofler, F., Zhao, S., Todorov, M., Rong, Z., Paetzold, J.C., Wiestler, B., et al. (2024). Virtual reality-empowered deep-learning analysis of brain cells. *Nat. Methods* 21, 1306–1315. <https://doi.org/10.1038/s41592-024-02245-2>.
21. Morigny, P., Kaltenecker, D., Zuber, J., Machado, J., Mehr, L., Tsokanos, F.F., Kuzi, H., Hermann, C.D., Voelkl, M., Monogarov, G., et al. (2021). Association of circulating PLA2G7 levels with cancer cachexia and assessment of darapladib as a therapy. *J. Cachexia Sarcopenia Muscle* 12, 1333–1351. <https://doi.org/10.1002/jcsm.12758>.
22. Morigny, P., Zuber, J., Haid, M., Kaltenecker, D., Riols, F., Lima, J.D.C., Simoes, E., Otoch, J.P., Schmidt, S.F., Herzig, S., et al. (2020). High levels of modified ceramides are a defining feature of murine and human cancer cachexia. *J. Cachexia Sarcopenia Muscle* 11, 1459–1475. <https://doi.org/10.1002/jcsm.12626>.
23. Loft, A., Alfaro, A.J., Schmidt, S.F., Pedersen, F.B., Terkelsen, M.K., Puglia, M., Chow, K.K., Feuchtinger, A., Troullinaki, M., Maida, A., et al. (2021). Liver-fibrosis-activated transcriptional networks govern hepatocyte reprogramming and intra-hepatic communication. *Cell Metab.* 33, 1685–1700.e9. <https://doi.org/10.1016/j.cmet.2021.06.005>.
24. Browaeys, R., Saelens, W., and Saeys, Y. (2020). NicheNet: modeling intercellular communication by linking ligands to target genes. *Nat. Methods* 17, 159–162. <https://doi.org/10.1038/s41592-019-0667-5>.
25. Baazim, H., Antonio-Herrera, L., and Bergthaler, A. (2022). The interplay of immunology and cachexia in infection and cancer. *Nat. Rev. Immunol.* 22, 309–321. <https://doi.org/10.1038/s41577-021-00624-w>.
26. Madsen, J.G.S., Rauch, A., Van Hauwaert, E.L., Schmidt, S.F., Winnefeld, M., and Mandrup, S. (2018). Integrated analysis of motif activity and gene expression changes of transcription factors. *Genome Res.* 28, 243–255. <https://doi.org/10.1101/gr.227231.117>.
27. Patke, A., Young, M.W., and Axelrod, S. (2020). Molecular mechanisms and physiological importance of circadian rhythms. *Nat. Rev. Mol. Cell Biol.* 21, 67–84. <https://doi.org/10.1038/s41580-019-0179-2>.
28. Takahashi, J.S. (2017). Transcriptional architecture of the mammalian circadian clock. *Nat. Rev. Genet.* 18, 164–179. <https://doi.org/10.1038/nrg.2016.150>.
29. Guan, D., Xiong, Y., Trinh, T.M., Xiao, Y., Hu, W., Jiang, C., Dierickx, P., Jang, C., Rabinowitz, J.D., and Lazar, M.A. (2020). The hepatocyte clock and feeding control chronophysiology of multiple liver cell types. *Science* 369, 1388–1394. <https://doi.org/10.1126/science.aba8984>.
30. Yan, Z., Yan, H., and Ou, H. (2012). Human thyroxine binding globulin (TBG) promoter directs efficient and sustaining transgene expression in

- p>liver-specific pattern.
- Gene*
- 506, 289–294.
- <https://doi.org/10.1016/j.gene.2012.07.009>
- .
31. Kalantar-Zadeh, K., Rhee, C., Sim, J.J., Stenvinkel, P., Anker, S.D., and Kovesdy, C.P. (2013). Why cachexia kills: examining the causality of poor outcomes in wasting conditions. *J. Cachexia Sarcopenia Muscle* 4, 89–94. <https://doi.org/10.1007/s13539-013-0111-0>.
 32. Kornmann, B., Schaad, O., Bujard, H., Takahashi, J.S., and Schibler, U. (2007). System-driven and oscillator-dependent circadian transcription in mice with a conditionally active liver clock. *PLoS Biol.* 5, e34. <https://doi.org/10.1371/journal.pbio.0050034>.
 33. Cho, H., Zhao, X., Hatori, M., Yu, R.T., Barish, G.D., Lam, M.T., Chong, L. W., DiTacchio, L., Atkins, A.R., Glass, C.K., et al. (2012). Regulation of circadian behaviour and metabolism by REV-ERB- α and REV-ERB- β . *Nature* 485, 123–127. <https://doi.org/10.1038/nature11048>.
 34. Jacobi, D., Liu, S., Burkewitz, K., Kory, N., Knudsen, N.H., Alexander, R.K., Unluturk, U., Li, X., Kong, X., Hyde, A.L., et al. (2015). Hepatic Bmal1 Regulates Rhythmic Mitochondrial Dynamics and Promotes Metabolic Fitness. *Cell Metab.* 22, 709–720. <https://doi.org/10.1016/j.cmet.2015.08.006>.
 35. Moser, A.R., Pitot, H.C., and Dove, W.F. (1990). A dominant mutation that predisposes to multiple intestinal neoplasia in the mouse. *Science* 247, 322–324. <https://doi.org/10.1126/science.2296722>.
 36. Puppa, M.J., White, J.P., Sato, S., Cairns, M., Baynes, J.W., and Carson, J.A. (2011). Gut barrier dysfunction in the Apc(Min/+) mouse model of colon cancer cachexia. *Biochim. Biophys. Acta* 1812, 1601–1606. <https://doi.org/10.1016/j.bbadis.2011.08.010>.
 37. Dumas, J.F., Goupille, C., Julienne, C.M., Pinault, M., Chevalier, S., Bougnoux, P., Servais, S., and Couet, C. (2011). Efficiency of oxidative phosphorylation in liver mitochondria is decreased in a rat model of peritoneal carcinosis. *J. Hepatol.* 54, 320–327. <https://doi.org/10.1016/j.jhep.2010.08.012>.
 38. Jones, A., Friedrich, K., Rohm, M., Schäfer, M., Algire, C., Kulozik, P., Seibert, O., Müller-Decker, K., Sijmonsma, T., Strzoda, D., et al. (2013). TSC22D4 is a molecular output of hepatic wasting metabolism. *EMBO Mol. Med.* 5, 294–308. <https://doi.org/10.1002/emmm.201201869>.
 39. Berriel Diaz, M., Krones-Herzig, A., Metzger, D., Ziegler, A., Vegiopoulos, A., Klingenspor, M., Muller-Decker, K., and Herzig, S. (2008). Nuclear receptor cofactor receptor interacting protein 140 controls hepatic triglyceride metabolism during wasting in mice. *Hepatology* 48, 782–791. <https://doi.org/10.1002/hep.22383>.
 40. Flint, T.R., Janowitz, T., Connell, C.M., Roberts, E.W., Denton, A.E., Coll, A.P., Jodrell, D.I., and Fearon, D.T. (2016). Tumor-Induced IL-6 Reprograms Host Metabolism to Suppress Anti-tumor Immunity. *Cell Metab.* 24, 672–684. <https://doi.org/10.1016/j.cmet.2016.10.010>.
 41. Zimmers, T.A., Fishel, M.L., and Bonetto, A. (2016). STAT3 in the systemic inflammation of cancer cachexia. *Semin. Cell Dev. Biol.* 54, 28–41. <https://doi.org/10.1016/j.semcdb.2016.02.009>.
 42. Webster, J.M., Kempen, L.J.A.P., Hardy, R.S., and Langen, R.C.J. (2020). Inflammation and Skeletal Muscle Wasting During Cachexia. *Front. Physiol.* 11, 597675. <https://doi.org/10.3389/fphys.2020.597675>.
 43. Braun, T.P., Grossberg, A.J., Krasnow, S.M., Levasseur, P.R., Szumowski, M., Zhu, X.X., Maxson, J.E., Knoll, J.G., Barnes, A.P., and Marks, D. L. (2013). Cancer- and endotoxin-induced cachexia require intact glucocorticoid signaling in skeletal muscle. *FASEB J.* 27, 3572–3582. <https://doi.org/10.1096/fj.13-230375>.
 44. Reinke, H., and Asher, G. (2016). Circadian Clock Control of Liver Metabolic Functions. *Gastroenterology* 150, 574–580. <https://doi.org/10.1053/j.gastro.2015.11.043>.
 45. Murayama, Y., Yahagi, N., Takeuchi, Y., Aita, Y., Mehrzad Saber, Z., Wada, N., Li, E., Piao, X., Sawada, Y., Shikama, A., et al. (2019). Glucocorticoid receptor suppresses gene expression of Rev-erb α (Nr1d1) through interaction with the CLOCK complex. *FEBS Lett.* 593, 423–432. <https://doi.org/10.1002/1873-3468.13328>.
 46. Verlande, A., Chun, S.K., Goodson, M.O., Fortin, B.M., Bae, H., Jang, C., and Masri, S. (2021). Glucagon regulates the stability of REV-ERB- α to modulate hepatic glucose production in a model of lung cancer-associated cachexia. *Sci. Adv.* 7, eabf3885. <https://doi.org/10.1126/sciadv.abf3885>.
 47. Masri, S., Papagiannakopoulos, T., Kinouchi, K., Liu, Y., Cervantes, M., Baldi, P., Jacks, T., and Sassone-Corsi, P. (2016). Lung Adenocarcinoma Distally Rewires Hepatic Circadian Homeostasis. *Cell* 165, 896–909. <https://doi.org/10.1016/j.cell.2016.04.039>.
 48. Yoshida, H., and Hunter, C.A. (2015). The immunobiology of interleukin-27. *Annu. Rev. Immunol.* 33, 417–443. <https://doi.org/10.1146/annurev-immunol-032414-112134>.
 49. Suh, D.S., and Rechler, M.M. (1997). Hepatocyte nuclear factor 1 and the glucocorticoid receptor synergistically activate transcription of the rat insulin-like growth factor binding protein-1 gene. *Mol. Endocrinol.* 11, 1822–1831. <https://doi.org/10.1210/mend.11.12.0021>.
 50. Sandri, M., Sandri, C., Gilbert, A., Skurk, C., Calabria, E., Picard, A., Walsh, K., Schiaffino, S., Lecker, S.H., and Goldberg, A.L. (2004). Foxo transcription factors induce the atrophy-related ubiquitin ligase atrogin-1 and cause skeletal muscle atrophy. *Cell* 117, 399–412. [https://doi.org/10.1016/s0092-8674\(04\)00400-3](https://doi.org/10.1016/s0092-8674(04)00400-3).
 51. Kwon, Y., Song, W., Droujinine, I.A., Hu, Y., Asara, J.M., and Perrimon, N. (2015). Systemic organ wasting induced by localized expression of the secreted insulin/IGF antagonist ImpL2. *Dev. Cell* 33, 36–46. <https://doi.org/10.1016/j.devcel.2015.02.012>.
 52. Bindels, L.B., Neyrinck, A.M., Loumaye, A., Catry, E., Walgrave, H., Cherbuy, C., Leclercq, S., Van Hul, M., Plovier, H., Pachikian, B., et al. (2018). Increased gut permeability in cancer cachexia: mechanisms and clinical relevance. *Oncotarget* 9, 18224–18238. <https://doi.org/10.18632/oncotarget.24804>.
 53. Molinaro, A., Koh, A., Wu, H., Schoeler, M., Faggi, M.I., Carreras, A., Hallén, A., Bäckhed, F., and Caesar, R. (2020). Hepatic expression of lipopolysaccharide-binding protein (Lbp) is induced by the gut microbiota through Myd88 and impairs glucose tolerance in mice independent of obesity. *Mol. Metab.* 37, 100997. <https://doi.org/10.1016/j.molmet.2020.100997>.
 54. Zhang, Y., Fang, B., Emmett, M.J., Damle, M., Sun, Z., Feng, D., Armour, S.M., Remsberg, J.R., Jager, J., Soccio, R.E., et al. (2015). GENE REGULATION. Discrete functions of nuclear receptor Rev-erb α couple metabolism to the clock. *Science* 348, 1488–1492. <https://doi.org/10.1126/science.aab3021>.
 55. Grimm, D., Kern, A., Rittner, K., and Kleinschmidt, J.A. (1998). Novel tools for production and purification of recombinant adenoassociated virus vectors. *Hum. Gene Ther.* 9, 2745–2760. <https://doi.org/10.1089/hum.1998.9.18-2745>.
 56. Gao, G.P., Alvira, M.R., Wang, L., Calcedo, R., Johnston, J., and Wilson, J. M. (2002). Novel adeno-associated viruses from rhesus monkeys as vectors for human gene therapy. *Proc. Natl. Acad. Sci. USA* 99, 11854–11859. <https://doi.org/10.1073/pnas.182412299>.
 57. Dobin, A., Davis, C.A., Schlesinger, F., Drenkow, J., Zaleski, C., Jha, S., Batut, P., Chaisson, M., and Gingeras, T.R. (2013). STAR: ultrafast universal RNA-seq aligner. *Bioinformatics* 29, 15–21. <https://doi.org/10.1093/bioinformatics/bts635>.
 58. Madsen, J.G.S., Schmidt, S.F., Larsen, B.D., Loft, A., Nielsen, R., and Mandrup, S. (2015). iRNA-seq: computational method for genome-wide assessment of acute transcriptional regulation from total RNA-seq data. *Nucleic Acids Res.* 43, e40. <https://doi.org/10.1093/nar/gku1365>.
 59. Love, M.I., Huber, W., and Anders, S. (2014). Moderated estimation of fold change and dispersion for RNA-seq data with DESeq2. *Genome Biol.* 15, 550. <https://doi.org/10.1186/s13059-014-0550-8>.
 60. Wu, T., Hu, E., Xu, S., Chen, M., Guo, P., Dai, Z., Feng, T., Zhou, L., Tang, W., Zhan, L., et al. (2021). clusterProfiler 4.0: A universal enrichment tool for interpreting omics data. *Innovation (Camb.)* 2, 100141. <https://doi.org/10.1016/j.xinn.2021.100141>.

61. Yu, G. (2020). Gene Ontology Semantic Similarity Analysis Using GOSem-Sim. *Methods Mol. Biol.* 2117, 207–215. https://doi.org/10.1007/978-1-0716-0301-7_11.
62. Li, H., and Durbin, R. (2009). Fast and accurate short read alignment with Burrows-Wheeler transform. *Bioinformatics* 25, 1754–1760. <https://doi.org/10.1093/bioinformatics/btp324>.
63. Li, H., Handsaker, B., Wysoker, A., Fennell, T., Ruan, J., Homer, N., Marth, G., Abecasis, G., and Durbin, R.; 1000 Genome Project Data Processing Subgroup (2009). The Sequence Alignment/Map format and SAMtools. *Bioinformatics* 25, 2078–2079. <https://doi.org/10.1093/bioinformatics/btp352>.
64. Heinz, S., Benner, C., Spann, N., Bertolino, E., Lin, Y.C., Laslo, P., Cheng, J.X., Murre, C., Singh, H., and Glass, C.K. (2010). Simple combinations of lineage-determining transcription factors prime cis-regulatory elements required for macrophage and B cell identities. *Mol. Cell* 38, 576–589. <https://doi.org/10.1016/j.molcel.2010.05.004>.
65. Quinlan, A.R., and Hall, I.M. (2010). BEDTools: a flexible suite of utilities for comparing genomic features. *Bioinformatics* 26, 841–842. <https://doi.org/10.1093/bioinformatics/btq033>.
66. Kent, W.J., Sugnet, C.W., Furey, T.S., Roskin, K.M., Pringle, T.H., Zahler, A.M., and Haussler, D. (2002). The human genome browser at UCSC. *Genome Res.* 12, 996–1006. <https://doi.org/10.1101/gr.229102>.
67. Gu, Z., Gu, L., Eils, R., Schlesner, M., and Brors, B. (2014). circlize Implements and enhances circular visualization in R. *Bioinformatics* 30, 2811–2812. <https://doi.org/10.1093/bioinformatics/btu393>.
68. Mo, A., Mukamel, E.A., Davis, F.P., Luo, C., Henry, G.L., Picard, S., Urich, M.A., Nery, J.R., Sejnowski, T.J., Lister, R., et al. (2015). Epigenomic Signatures of Neuronal Diversity in the Mammalian Brain. *Neuron* 86, 1369–1384. <https://doi.org/10.1016/j.neuron.2015.05.018>.
69. Postic, C., Shiota, M., Niswender, K.D., Jetton, T.L., Chen, Y., Moates, J. M., Shelton, K.D., Lindner, J., Cherrington, A.D., and Magnuson, M.A. (1999). Dual roles for glucokinase in glucose homeostasis as determined by liver and pancreatic beta cell-specific gene knock-outs using Cre recombinase. *J. Biol. Chem.* 274, 305–315. <https://doi.org/10.1074/jbc.274.1.305>.
70. Evans, W.J., Morley, J.E., Argilés, J., Bales, C., Baracos, V., Guttridge, D., Jatoi, A., Kalantar-Zadeh, K., Lochs, H., Mantovani, G., et al. (2008). Cachexia: a new definition. *Clin. Nutr.* 27, 793–799. <https://doi.org/10.1016/j.clnu.2008.06.013>.
71. Fearon, K., Strasser, F., Anker, S.D., Bosaeus, I., Bruera, E., Fainsinger, R. L., Jatoi, A., Loprinzi, C., MacDonald, N., Mantovani, G., et al. (2011). Definition and classification of cancer cachexia: an international consensus. *Lancet Oncol.* 12, 489–495. [https://doi.org/10.1016/S1470-2045\(10\)70218-7](https://doi.org/10.1016/S1470-2045(10)70218-7).
72. Jamal-Hanjani, M., Wilson, G.A., McGranahan, N., Birkbak, N.J., Watkins, T.B.K., Veeriah, S., Shafi, S., Johnson, D.H., Mitter, R., Rosenthal, R., et al. (2017). Tracking the Evolution of Non-Small-Cell Lung Cancer. *N. Engl. J. Med.* 376, 2109–2121. <https://doi.org/10.1056/NEJMoa1616288>.
73. Frankell, A.M., Dietzen, M., Al Bakir, M., Lim, E.L., Karasaki, T., Ward, S., Veeriah, S., Colliver, E., Huebner, A., Bunkum, A., et al. (2023). The evolution of lung cancer and impact of subclonal selection in TRACERx. *Nature* 616, 525–533. <https://doi.org/10.1038/s41586-023-05783-5>.
74. Al-Sawaf, O., Weiss, J., Skrzypski, M., Lam, J.M., Karasaki, T., Zambrana, F., Kidd, A.C., Frankell, A.M., Watkins, T.B.K., Martínez-Ruiz, C., et al. (2023). Body composition and lung cancer-associated cachexia in TRACERx. *Nat. Med.* 29, 846–858. <https://doi.org/10.1038/s41591-023-02232-8>.
75. Schäfer, M., Oeing, C.U., Rohm, M., Baysal-Temel, E., Lehmann, L.H., Bauer, R., Volz, H.C., Boutros, M., Sohn, D., Sticht, C., et al. (2016). Ataxin-10 is part of a cachexokine cocktail triggering cardiac metabolic dysfunction in cancer cachexia. *Mol. Metab.* 5, 67–78. <https://doi.org/10.1016/j.molmet.2015.11.004>.
76. Oeing, C.U., Pepin, M.E., Saul, K.B., Agircan, A.S., Assenov, Y., Merkel, T. S., Sedaghat-Hamedani, F., Weis, T., Meder, B., Guan, K., et al. (2023). Indirect epigenetic testing identifies a diagnostic signature of cardiomyocyte DNA methylation in heart failure. *Basic Res. Cardiol.* 118, 9. <https://doi.org/10.1007/s00395-022-00954-3>.
77. Fellmann, C., Hoffmann, T., Sridhar, V., Hopfgartner, B., Muhar, M., Roth, M., Lai, D.Y., Barbosa, I.A.M., Kwon, J.S., Guan, Y., et al. (2013). An optimized microRNA backbone for effective single-copy RNAi. *Cell Rep.* 5, 1704–1713. <https://doi.org/10.1016/j.celrep.2013.11.020>.
78. Team, R.C. (2021). R: A Language and Environment for Statistical Computing (R Foundation for Statistical Computing).

STAR★METHODS

KEY RESOURCES TABLE

REAGENT or RESOURCE	SOURCE	IDENTIFIER
Antibodies		
anti-GFP antibody	Life Technologies	Cat#: G10362; RRID: AB_2536526
anti-BMAL1	Abcam	Cat#: ab93806; RRID: AB_10675117
anti-REV-ERB α	gift from Ronald Evans (Salk Institute for Biological Sciences)	N/A
anti-GFP antibody	Santa Cruz	Cat#: sc-8334; RRID: AB_641123
anti-LBP	R&D Systems	Cat#: AF6635; RRID: AB_10973622
anti-ITIH3	Sigma-Aldrich	Cat#: SAB2700465
anti- β -Actin	Sigma-Aldrich	Cat#: A5441; RRID: AB_476744
anti-Vinculin	Abcam	Cat#: ab129002; RRID: AB_11144129
Anti-Lamin A/C (4C11)	Cell Signaling	Cat#: 4777; RRID: AB_10545756
anti-sarcomeric α -Actinin antibody	Sigma-Aldrich	Cat#: A7811; RRID: AB_476766
anti-LBP	R&D Systems	Cat#: MAB6635; RRID: AB_3658625
anti-ITIH3	Thermo Fisher	Cat#: 21247-1-AP; RRID: AB_2878830
anti-IGFBP1	R&D Systems	Cat#: MAB675; RRID: AB_2122946
rat IgG	R&D Systems	Cat#: 6-001-F; RRID: AB_2616570
mouse IgG	R&D Systems	Cat#: MAB002R; RRID: AB_3657051
rabbit IgG	R&D Systems	Cat#: AB-105-C; RRID: AB_354266
Goat anti-Mouse IgG (H+L) Highly Cross-Adsorbed Secondary Antibody, Alexa Fluor™ 594	Thermo Fisher	Cat#: A-11032; RRID: AB_2534091
Anti-mouse IgG, HRP-linked Antibody	Cell Signaling	Cat#: 7076; RRID: AB_330924
Sheep IgG Horseradish Peroxidase-conjugated Antibody	R&D Systems	Cat#: HAF016; RRID: AB_562591
Goat Anti-Rabbit IgG (H+L)-HRP Conjugate	Bio Rad	Cat#:1721019; RRID: AB_11125143
Bacterial and virus strains		
AAV-TBG-REV-ERB α (serotype AAV2/8)	Vigene	Custom production with Vigene
AAV-TBG-GFP (serotype AAV2/8)	Vigene	Custom production with Vigene
AAV-TBG-shControl (serotype AAV8)	This study; VectorBuilder	Custom production with VectorBuilder
AAV-TBG-shLbp (serotype AAV8)	This study; VectorBuilder	Custom production with VectorBuilder
AAV-TBG-shItih3 (serotype AAV8)	This study; VectorBuilder	Custom production with VectorBuilder
AAV-TBG-shLbp_shItih3 (serotype AAV8)	This study; VectorBuilder	Custom production with VectorBuilder
AAV-TBG-shIGFBP1 (serotype AAV8)	This study; VectorBuilder	Custom production with VectorBuilder
Chemicals, peptides, and recombinant proteins		
recombinant mouse LBP protein	R&D Systems	Cat#: 6635-LP
recombinant human ITIH3 protein	Biomol	Cat#: E-PKSH032658
recombinant mouse IGFBP1 protein	R&D Systems	Cat#: 1588-B1
CXCL14/BRAX protein	R&D Systems	Cat#: #730-XC
PhosSTOP	Sigma-Aldrich	Cat#: 4906845001
TRIzol	Life Technologies	Cat#: 15596018
EDTA-free Protease Inhibitor Cocktail	Roche	Cat#: 11873580001
RNasin Plus Rnase Inhibitor	Promega	Cat#: N2615
Protein G Dynabeads	Life Technologies	Cat#: 10004D
DAPI	Sigma	Cat#: D9542

(Continued on next page)

Continued

REAGENT or RESOURCE	SOURCE	IDENTIFIER
DAPI	Thermo Fisher	Cat#: D1306
Critical commercial assays		
Free Glycerol Reagent	Sigma-Aldrich	Cat#: F6428
Mouse IGFBP1 ELISA	Abcam	Cat#: ab272465
Human IGFBP-1 DuoSet ELISA	R&D Systems	Cat#: #DY871
ProcartaPlex multiplex ELISA for detection of IL-6, TNF α , IL-1 β , IL-27 and IL-22	Thermo Fisher	Custom panel design
Deposited data		
Whole liver and hepatocyte (INTACT) RNA-seq data	This study	GEO: GSE293096
Hepatocyte (INTACT) ATAC-seq data	This study	GEO: GSE293099
Heart RNA-Seq data	This study	GEO: GSE293093
Original code	This study	Zenodo: https://doi.org/10.5281/zenodo.15492701
Western blot images	This study	Zenodo: https://doi.org/10.5281/zenodo.15492701
Experimental models: Cell lines		
Murine C26 colon cancer cells	German Cancer Research Center (Deutsches Krebsforschungszentrum, DKFZ Tumorbank)	N/A
Murine NC26 colon cancer cell	NC26 cells were kindly provided by Rudolf Zechner and Martina Schweiger from the Institute of Molecular Biosciences (University of Graz) and were originally obtained from the Cell Resource Center for Biomedical Research-Cell Bank of the Tohoku University (TKG-0518).	N/A
Murine 8025 PDAC cells	derived from KPC (KrasLSL-G12D; Trp53LSL-R172H; Pdx1-Cre) mice (a kind gift of gift from Dieter Saur, TU Munich, Germany)	N/A
Murine MC38 colon cancer cells	Merck-Millipore	Cat#: SCC172; RRID: CVCL_B288
Murine Lewis Lung Carcinoma cells	ATCC	Cat#: CRL-1642; RRID: CVCL_4358
C2C12 cells	ATCC	Cat#: CRL-1772; RRID: CVCL_0188
immortalized stroma vascular fraction (SVF) of murine inguinal WAT for adipocyte differentiation	This study	N/A
Experimental models: Organisms/strains		
C57BL/6J	Charles River	Strain code: 632
BALB/cAnNCrl	Charles River	Strain code: 028
C57BL/6NCrl	Charles River	Strain code: 027
B6;129 Gt(ROSA)26Sor ^{tm5(CAG-Sun1/sfGFP)Nat/J}	JAX	Strain code: 021039
B6N.Cg-Speer6-ps1 ^{Tg(Alb-cre)21Mgn/J}	JAX	Strain code: 003574
C57BL/6J-Apc ^{Min} /J	JAX	Strain code: 002020
B6.129S4(Cg)-Bmal1 ^{tm1Weit/J}	JAX	Strain code: 007668
C.Cg-Gt(ROSA)26Sor ^{tm5(CAG-Sun1/sfGFP)Nat/J} Sszg	This study	N/A
C.Cg-Speer6-ps1 ^{Tg(Alb-cre)21Mgn/J} Sszg mice	This study	N/A
Oligonucleotides		
qPCR Primer: Lbp_1: TCCATCGGTGTCCGAGGCAAAT	This paper	N/A

(Continued on next page)

Continued

REAGENT or RESOURCE	SOURCE	IDENTIFIER
qPCR Primer: Lbp_2: (AGGTCCACTGAAATGGTGACACC)	This study	N/A
qPCR Primer: Itih3_1 (CTCTTCAGCACCGATGTGACCA)	This study	N/A
qPCR Primer: Itih3_2 (ACCCCTTCAGCAGCCCATTG)	This study	N/A
qPCR Primer: Igfbp1_1 (GCCCCAACAGAAAGCAGGAGATG)	This study	N/A
qPCR Primer: Igfbp1_2 (GTAGACACACCAGCAGAGTCCA)	This study	N/A
qPCR Primer: Arntl_1 (GCAGTGCCACTGACTACCAA)	This study	N/A
qPCR Primer: Arntl_2 (GCAGTGCCACTGACTACCAA)	This study	N/A
qPCR Primer: Nr1d1_1 (CAGGCTTCCGTGACCTTCTCA)	This study	N/A
qPCR Primer: Nr1d1_2 (TAGGTTGTGCGGCTCAGGAACA)	This study	N/A

Recombinant DNA

pAAV.TBG.PI.eGFP.WPRE.bGH	Addgene	Addgene plasmid #105535; RRID: Addgene_105535
pAAV-TBG-REV-ERB α	a gift from Mitchell Lazar, University of Pennsylvania ⁵⁴	N/A
pDGDVP	a gift from Jürgen Kleinschmidt, DKFZ Heidelberg ⁵⁵	N/A
p5E18-VD2/8	a gift from Jürgen Kleinschmidt, DKFZ Heidelberg ⁵⁶	N/A

Software and algorithms

STAR aligner	Dobin et al. ⁵⁷	v2.4.2a
iRNA-seq	Madsen et al. ⁵⁸	v1.1
DESeq2	Love et al. ⁵⁹	v1.24.0
Uniprot.org	https://www.uniprot.org/	N/A
clusterProfiler	Wu et al. ⁶⁰	v4.6.2
GOSemSim	Yu ⁶¹	v2.24.0
NicheNetR	Browaeys et al. ²⁴	v2.0.0
IMAGE	Madsen et al. ²⁶	v1.1
BWA	Li and Durbin ⁶²	v0.7.5a-r405
Samtools	Li et al. ⁶³	v0.1.19
HOMER	Heinz et al. ⁶⁴	v4.10
bedtools	Quinlan and Hall ⁶⁵	v2.29

UCSC Genome Browser	http://genome.ucsc.edu , ⁶⁶	N/A
Circlize (R package)	Gu et al. ⁶⁷	v0.4.15

Other

EconoSpin Micro/Mini Columns	Epoch Life Science	Cat#: 3010-250/1920-250
High glucose DMEM	Thermo Fisher	Cat#: 41966052
Fetal bovine serum	Sigma-Aldrich	Cat#: F7524
Penicillin-streptomycin	Thermo Fisher	Cat#: 15140122
High glucose DMEM, no calcium, no glutamine	Thermo Fisher	Cat#: 21068028
DMEM/F-12, GlutaMAX	Thermo Fisher	Cat#: 10565018

EXPERIMENTAL MODEL AND STUDY PARTICIPANT DETAILS

Animal models

Animal experimentation was performed in accordance with the European Union directives and the German animal welfare act (Tierschutzgesetz). They have been approved by the state ethics committee and the government of Upper Bavaria (ROB-55.2-2532.Vet_02-16-136, ROB-55.2-2532.Vet_02-18-93 and ROB-55.2-2532.Vet_02-22.47).

B6;129 *Gt(ROSA)26Sor^{tm5(CAG-Sun1/sfGFP)Nat}/J* mice⁶⁸ were backcrossed to C57BL/6NCrI (B6/N) using a speed congenics approach to ensure a > 95 % genetic B6/N background. These were then crossed with B6N.Cg-*Speer6-ps1^{Tg(Alb-cre)21Mgn}/J* (Alb-Cre) mice⁶⁹ to generate HEP-INTACT mice with hepatocyte-specific GFP tagging of the nuclear membrane on a B6N background (HEP-INTACT-B6). In addition, B6;129 *Gt(ROSA)26Sor^{tm5(CAG-Sun1/sfGFP)Nat}/J* mice⁶⁸ and B6N.Cg-*Speer6-ps1^{Tg(Alb-cre)21Mgn}/J* (Alb-Cre)⁶⁹ were backcrossed to BALB/c using a speed congenics approach to ensure a >95 % genetic BALB/c background, yielding in C.Cg-Gt(ROSA)26Sor^{tm5(CAG-Sun1/sfGFP)Nat}/JSszg and C.Cg-*Speer6-ps1^{Tg(Alb-cre)21Mgn}/JSszg* mice. The resulting mouse lines were then intercrossed to generate HEP-INTACT mice with hepatocyte-specific GFP tagging of the nuclear membrane on a BALB/c background (HEP-INTACT-BALB/c). Mice were maintained on a 12-h light–dark cycle and fed a regular unrestricted chow diet. Male mice were used for experiments at an age of 10–12 weeks. Experimental mice were sacrificed between 2:30 – 3:30 p.m. (~ZT9).

HEP-INTACT-B6 mice were injected with 1×10^6 MC38 in 50 μ l PBS:Matrigel (1:1) subcutaneously into the right flank or orthotopically into the pancreas with 3000 pancreatic 8025 cancer cells in 20 μ l PBS:Matrigel (1:1). For orthotopic pancreas injections, mice were anesthetized with a mix of ketamine/xylazine before transplantation. HEP-INTACT-BALB/c mice were injected with 1×10^5 C26 or 1.5×10^6 NC26 cells in 50 μ l PBS:Matrigel (1:1) subcutaneously into the right flank. Control mice were injected with corresponding volumes of PBS:Matrigel. 5 days after cell implantation, mice were monitored daily for tumor growth and body weight. C26 or 8025 tumor-bearing mice were considered cachectic when they had lost 10% - 15% of body weight. Pre-cachexia in C26 tumor-bearing mice was defined a non-significant loss of body weight at the moment of sacrifice in the presence of an established tumor. Mice were sacrificed at Zeitgeber Zeit (ZT) 9 (referring to 3pm) by cervical dislocation and tissues and organs were dissected and weighed.

For AAV-mediated overexpression of REV-ERB α , male BALB/c mice (Charles River, Brussels) were used at an age of 10-12 weeks. Mice were injected with 5×10^{11} GC/ml AAVs for overexpression of REV-ERB α (TBG-REV-ERB α) or GFP as control (TBG-GFP) under the hepatocyte-specific TBG promoter. Ten days later, 1×10^5 C26 cells in 50 μ l PBS:Matrigel (1:1) were subcutaneously injected into the right flank. Control mice received a PBS:Matrigel (1:1) injection. Body weight and tumor development was monitored as described above. Mice were sacrificed at ZT 9.

For AAV-mediated knockdown of LBP, ITIH3 and IGFBP1, male BALB/c mice (Charles River, Brussels) were used at an age of 10–12 weeks. Mice were injected with 5×10^{11} GC/ml AAVs for hepatocyte-specific expression of shRNAs under the TBG promoter to knockdown Lbp (TBG-shLbp), Itih3 (TBG-shItih3), Igfbp1 (TBG-shIgfbp1) or a scramble control (TBG-shControl) via the tail vein. 14 days later, 1×10^6 C26 cells in 50 μ l PBS were subcutaneously injected into the right flank. Control mice received a PBS injection. Body weight and tumor development was monitored as described above. Mice were sacrificed at ZT 9. Forelimb grip strength was measured using a grip strength tester (Bioseb, Vitrolles, France).

Apc^{Min/+} mice^{35,36} were purchased from the Jackson Laboratory (JAX stock #002020) and bred on a C57BL/6J background carrying floxed alleles of *Arntl*.³⁴ Male mice were monitored and sacrificed once end-point criteria were reached at 3–6 months of age. For the LLC model, male C57BL/6J mice (Charles River, Brussels) carrying floxed alleles of *Arntl* were subcutaneously transplanted with 1 million LLC cells subcutaneously to the right flank at an age of 10-12 weeks. Body weight and tumor development was monitored until an endpoint criterion was reached. Mice were sacrificed at ZT 9. Liver-specific *Arntl1* knockout mice were generated by crossing albumin-cre transgene to *Arntl1* f/f mice³⁴ and male mice were used at an age of 11-12 weeks of age.

Patient cohorts and samples

Patient cohort 1

Male and female gastrointestinal cancer patients (stages I–IV) were enrolled at the Surgical Clinic of the University Hospital of São Paulo after signature of the fully informed consent.²² This study was approved by the Ethics Committee on Research Involving Human Subjects of the University of the São Paulo Biomedical Sciences Institute (CEP 1151/13 CAAE n 5493116.6.0000467) and by the University Hospital (CEP 1390/14 CAAE n 54930116.6.3001.0076) and is in accordance with the Declaration of Helsinki. Exclusion criteria: BMI > 29.9 kg/m², chronic anti-inflammatory therapy or chronic inflammatory processes not related to cachexia, chemotherapy treatment (at the time or recent past 5 years), AIDS, or liver or kidney failure. Approximately 20 mL of blood were collected in pre-surgical fast at the hospital. Biochemical analysis was performed with the automatic LABMAX 240® equipment (Labtest, Lagoa Santa, Brazil) using commercial kits. Haemoglobin concentration was obtained from the hospital records, before the surgery. Cancer patients were classified as weight-stable (Ws) or cachectic (Cx), following Evans et al.⁷⁰ Additional information including the age of the patients can be found in [Table S1](#).

Patient cohort 2

Enrolment of Munich male and female pancreatic cancer patients (Stages I–IV) occurred in the Department of Surgery, Klinikum Rechts der Isar.²¹ This study was approved by the Ethics Committee of the Medical Faculty of the Technical University of Munich (Germany; #1946/07 and #409/16S), and written informed consent was obtained from all participants before surgery or before blood sampling. The analysis was conducted on a pseudonymized data set. The study population comprised patients with pancreatic

cancer, who underwent oncological treatment (staging or resection) and who agreed to participate in the study. Diagnosis of pancreatic cancer patients was verified by definitive histological examination of retrieved biopsies, or in pancreatic cancer patients without surgery, by cytology or clinical/radiological information to the best of our knowledge. We used the eighth edition of the Union for International Cancer Control tumour–node–metastasis classification and staging system for pancreatic cancer. Weight was measured at the time of admission to the hospital. Weight histories over the 6 months preceding admission were collected. Cachexia was defined according to Fearon et al.⁷¹ Weight-stable patients were defined as those not meeting Fearon’s criteria for cachexia. Additional information including the age of the patients can be found in Table S2.

Patient cohort 3

TRACERx is a UK-wide prospective multicenter observational cohort study in male and female participants with early-stage non-small cell lung cancer that aims to characterize tumor evolution through multi-regional and longitudinal tumor sampling (NCT01888601). The TRACERx study has been approved by an independent research ethics committee (13/LO/1546) and informed consent was obtained from every patient. The study protocol with inclusion/exclusion criteria has been described previously.^{72,73} The plasma proteome in the TRACERx cohort was profiled using the Olink Explore 3072 panel as previously described.⁷⁴ Normalized protein expression (NPX) values in samples obtained at disease recurrence were compared between cachexia and non-cachexia groups after excluding study participants that develop new primary tumors during the time of follow-up. Cachexia was defined as a weight loss of more than 5% between patient weight at baseline and weight at relapse, or a weight loss of more than 2% if the baseline body mass index (BMI) was lower than 20 kg/m². Additional information including the age of the patients can be found in Table S3.

METHOD DETAILS

Cell culture

The murine colon cancer cell lines MC38, NC26, C26 as well as the murine pancreatic ductal adenocarcinoma cell line 8025⁷⁵ derived from KPC (KrasLSL-G12D; Trp53LSL-R172H; Pdx1-Cre) mice (a kind gift of gift from Dieter Saur, TU Munich, Germany) and murine lung cancer cell line LLC were cultured in high glucose DMEM with pyruvate (Life Technologies #41966052), supplemented with 10% fetal bovine serum (Sigma-Aldrich #F7524) and 1% penicillin-streptomycin (Thermo Fisher #15140122) as previously described.²¹ Before using the cells for transplantation, cells had a confluence of 80%. Cells were trypsinized, counted and required cell numbers were suspended in Dulbecco’s phosphate-buffered saline (PBS, Thermo Fisher #14190250).

C2C12 cells (ATCC #CRL-1772) were grown in high-glucose DMEM with pyruvate supplemented with 10% FBS and 1% penicillin-streptomycin. To induced myotube differentiation, cells were placed in differentiation medium (high-glucose DMEM with pyruvate supplemented with 2% FBS and 1% penicillin-streptomycin) when they reached 80–100% confluence. The differentiation medium was exchanged every two days until myotubes were differentiated after 5 days.

Primary neonatal rat cardiomyocytes were isolated from Wistar rats at an age of 1–2 days as previously described.⁷⁶ Cells were cultured on culture plates coated with 0.1% gelatin in high glucose DMEM supplemented with 10% FBS and 1% penicillin-streptomycin.⁷⁵

For adipocyte culture, we isolated and immortalized the stroma vascular fraction (SVF) of murine inguinal WAT (iWAT) using standard procedures. Briefly, iWAT depots of 12-week old male C57BL/6J mice were minced and incubated in digestion medium (DMEM/F12, Glutamax, 0.15% (w/v) Collagenase D, and 2% BSA) at 37°C for 40 min. Digested tissue was filtered through a 100 µm filter, rinsed with DMEM/F12, and centrifuged at 500g for 5min. Cells were re-suspended in DMEM/F12 and filtered through 40 µm filter, followed by 5 min centrifugation at 500g. The Cell pellet was resuspended in growth medium (DMEM/F12 Glutamax, 10% FCS, 1% penicillin/streptomycin) plated and cultured. After 24 hours, pre-adipocytes were immortalized using SV40 large T-antigen (provided by Dr. Siegfried Ussar, Helmholtz Munich). After 48–72 hours, cells were split into new flasks, cultured until 70% confluence, and frozen in freeze medium (growth medium, 50% FCS, and 10% DMSO). For differentiation, 10,000 cells were seeded in a 96-well plate in a total volume of 100 µl. Two days after seeding, differentiation was started adding induction medium (DMEM/F12 Glutamax, 10 µg/ml Insulin, 2 µM Rosiglitazone, 0.25 µM Dexamethasone, and 0.5 mM IBMX). After 3 days, medium was changed and replaced by growth medium containing 10 µg/ml insulin. From day 5–9, growth medium containing 0.5 µg/ml insulin was added and medium was changed once at day 7. Afterwards, cells were kept in growth medium without insulin for two days before being used for the treatment with recombinant proteins on day 11.

Generation of adeno associated virus (AAV)

pAAV.TBG.PI.eGFP.WPRE.bGH (pAAV-GFP) was a gift from James M. Wilson (Addgene plasmid #105535; <http://n2t.net/addgene:105535>; RRID:Addgene_105535), and pAAV-TBG-REV-ERBα was a gift from Mitchell Lazar, University of Pennsylvania.⁵⁴ AAV packaging and titer determination by qPCR against viral genomes was performed by Vigene, using the pGDVP helper plasmid⁵⁵ and a mutated p5E18-VD2/8 expression vector⁵⁶ encoding AAV2 rep and a mutated AAV8 cap protein (aa 589–592: QNTA to GNRQ).

For hepatocyte-specific knockdowns of hepatokines *Lbp*, *lith3* and *Igf1bp1*, we utilized the miR30-based shRNA knockdown vector system in combination with the hepatocyte specific promoter TBG (pAAV[miR30]-TBG>EGFP:(shRNA):WPRE) from

VectorBuilder, which allows shRNAs to be transcribed in a hepatocyte specific manner.⁷⁷ Following shRNA guide sequences were used for *Lbp*: TGAAGTTTCAGGAAGGATTGTC; *Itih3*: TGAAGTGGTGATCTTTCCAGG; *Igfbp1*: TTTACATGTACAGAGATGAGAA; CTATAGGTGCTGATGGCGTTCC, and ATGTCTCACACTGTTTGCTGTG; Control: CGAGGGCGACTTAACCTTAGGT.

Isolation of GFP-tagged nuclei

Liver tissue from INTACT mice was rapidly dissected in PBS and snap-frozen in liquid nitrogen. GFP+ hepatocyte nuclei were enriched using the INTACT liver protocol as previously described.¹⁸ In brief, liver tissue was crushed into fine powder using a TissueLyzer II (Qiagen) and subsequently washed in PBS. The tissue was Dounce homogenized using 10× loose pestle in 5 mL of low sucrose buffer (LSB: 0.25 M sucrose, 25 mM KCl, 5 mM MgCl₂, 20 mM Tris-HCl (pH 7.5), 1 mM 1,4-dithiothreitol (DTT), 0.15 mM spermine, 0.5 mM spermidine, 1× EDTA-free protease inhibitor cocktail (PIC) (Roche), and 60 U/mL RNasin Plus RNase Inhibitor (Promega)) per 0.5 mg of tissue, then added 0.35 % Igepal CA-630 (Sigma) and left on ice for 5 min followed by further douncing 5× with the tight pestle. The homogenate was filtered through a 100 μm CellTrics filter unit (Sysmex Deutschland) and spun down at 4°C, 600g for 10 min. The pellet was resuspended in 9× high sucrose buffer (same as LSB, but with 2 M sucrose) and centrifuged 15,000g for 15 min at 4°C. The nuclei pellet was subsequently resuspended in wash buffer (LSB with 0.35 % Igepal CA-630) and an aliquot of whole liver nuclei was kept on ice for later analyses. Pre-clearing of nuclei (15 mill nuclei per HEP-INTACT mouse) was done by incubating with 20 μL of Protein G Dynabeads (Life Technologies) for 15 min. After removal of the beads on a magnet, the solution was incubated with 3 μg rabbit monoclonal anti-GFP antibody (Life Technologies) for 30 min. Then 80 μL of Dynabeads was added and the solution was incubated for additional 20 min. Bead-bound nuclei were washed 3× in 2 mL wash buffer (without RNasin) using a magnet. All steps were performed on ice or in the cold room, and all incubations were carried out using an end-to-end rotator.

Tissue RNA isolation and quantitative PCR

For RNA isolation from tissue, ~200 mg of liver, GC muscle or heart tissue was lysed in Trizol using the TissueLyser II (Qiagen, #85300) followed by RNA purification using EconoSpin columns (Epoch). RNA concentrations were determined using the Nanodrop 2000 (Thermo Fisher).

cDNA was transcribed using the QuantiTect Reverse Transcription Kit (Qiagen, #205313) according to the protocol of the manufacturer. Quantitative real time PCR was performed using the TaqMan Gene Expression Master Mix (Life Technologies, #4369514) or the SYBR Green PCR Master Mix (Life technologies) on QuantStudio 6 and 7 Flex Real-Time PCR System (Applied Biosystems). Relative RNA expression was quantified using the ΔCt method and normalized to the TATA-box binding protein RNA (Tbp, Mm01277042_m1). The following TaqMan probes (Applied Biosystems) were used: Foxo3 (Mm01185722_m1), Trim63 (Mm01185221_m1), Fbxo32 (Mm00499523_m1), Map1lc3b (Mm00782868_sH), Bnip3 (Mm01275600_g1). In addition, we used following primer combinations: *Lbp_1* (TCCATCGGTGTCCGAGGCAAAT) and *Lbp_2* (AGGTCCACTGAAATGGTGACACC); *Itih3_1* (CTCTTCAGCACCGATGTGACCA) and *Itih3_2* (ACCCTTCAGCAGCCCATCATTG); *Igfbp1_1* (GCCCAACAGAAAGCAGGAGATG) and *Igfbp1_2* (GTAGACACACCAGCAGAGTCCA); *Arntl_1* (GCAGTGCCACTGACTACCAA) and *Arntl_2* (GCAGTGCCACTGACTACCAA); *Nr1d1_1* (CAGGCTTCCGTGACCTTTCTCA) and *Nr1d1_2* (TAGGTTGTGCGGCTCAGGAACA).

RNA-seq from nuclei: isolation to sequencing

Whole-liver nuclei and bead-bound nuclei prepared from INTACT mice were directly resuspended in Trizol (Life Technologies, #15596018), and RNA purification was performed using EconoSpin columns (Epoch) with on-column DNase digestion (Qiagen) as described in Loft et al.¹⁸ Total RNA (50–100 ng) was prepared for sequencing using VAHTS Stranded mRNA-seq Library Kit for Illumina (Vazyme) following manufacturer's recommendations, except that no selection for poly-adenylated RNA was performed. Library quality was assessed on the Agilent Bioanalyzer 2100 system. The prepared libraries were sequenced (paired-end) on an Illumina HiSeq 4000 platform.

ATAC-seq library construction and sequencing

Approximately 25,000 bead-bound nuclei from INTACT animals were transposed in a 50 μL volume of 1X TTBL buffer and 3.5 μL TTE Mix V50 (from TruePrep DNA Library Prep Kit V2 for Illumina, Vazyme) for 30 minutes at 37°C. Fragmented genomic DNA was recovered using Buffer ERC coupled with MinElute spin column purification (Qiagen). Transposed genomic DNA was amplified by 12–14 cycles of quantitative PCR. Amplified DNA was purified and size-selected on AMPure XP beads (Beckman), analyzed on an Agilent Bioanalyzer, and sequenced (paired-end) on an Illumina HiSeq 4000 platform.

Western Blot

Liver and heart protein lysates were prepared by homogenizing frozen tissue (~200 mg) in RIPA buffer with freshly added inhibitors (1× EDTA-free protease inhibitor, and 1× PhosSTOP) using the TissueLyzer II (Qiagen). Samples were centrifuged at 13,000 g and 4°C for 45 minutes. Protein content of cleared lysates was determined using the Pierce BCA Kit (Thermo Fisher Scientific, #23225). 50 μg protein were incubated with 6× Laemmli buffer at 95°C for 5 minutes before loading it on an SDS-PAGE gel (Novex WedgeWell, Tris-Glycine Mini Gels; Thermo Fisher Scientific, or Mini-PROTEAN Precast Gels; Bio-Rad Laboratories). For human and mouse plasma samples, 1 μL of plasma was mixed with 415 μL of water with freshly added inhibitors (1× EDTA-free protease inhibitor, and 1× PhosSTOP). 10 μL of this dilution was mixed with 2 μL 6× Laemmli buffer and incubated at 37°C for 7 minutes before loading it on

an SDS-PAGE gel. Gels were run at 100–120V and subsequently transferred to a nitrocellulose membrane (Bio-Rad). Membranes were blocked with 5% skimmed milk in TBS-T and incubated with primary antibodies against BMAL1 (Abcam, #ab93806), GFP (Santa Cruz, #sc-8334), LBP (R&D systems, #AF6635), ITIH3 (Sigma-Aldrich, SAB2700465) or REV-ERB α (custom antibody produced by the Ronald Evans lab) diluted in 5% skimmed milk in TBS-T or 5% bovine serum albumin.

Anti-rabbit, anti-mouse or anti-sheep (R&D systems, HAF016) IgG coupled to horseradish peroxidase were used at a dilution of 1:10,000 in 5% milk as secondary antibodies, and immunoreactive proteins were determined by chemiluminescence using a ChemiDoc MP System (Bio-Rad).

ELISA

ELISA was used to determine plasma levels of IGFBP1 (Mouse IGFBP1 ELISA kit from Abcam, #ab272465; Human IGFBP-1 DuoSet ELISA from R&D Systems, #DY871). Plasma IL-6, TNF α , IL-1 β , IL-27 and IL-22 were measured using the ProcartaPlex multiplex ELISA (Thermo Fisher).

Myotube treatment and diameter analysis

C2C12 myotubes were treated with the indicated doses of recombinant proteins for 48h, at which the media (high-glucose DMEM with pyruvate supplemented with 2% FBS and 1% penicillin–streptomycin) with freshly added recombinant protein was renewed after 24h. Consequently, cells were washed once with PBS and PFA fixed over-night. Wells were imaged ($\times 20$ or $\times 40$ objective, #Nikon Eclipse Ts2) and myotube diameters were measured using ImageJ. Following recombinant proteins were purchased from commercial providers: recombinant mouse LBP protein (R&D Systems, #6635-LP), recombinant human ITIH3 protein (Biomol, #E-PKSH032658), recombinant mouse IGFBP1 protein (R&D Systems, #1588-B1) and recombinant mouse CXCL14/BRAK protein (R&D Systems, #730-XC).

Cardiomyocyte treatment and size quantification

Primary rat cardiomyocytes were treated with the indicated doses of recombinant protein (for providers, see above) for 24h. Immunofluorescence-aided high-throughput analysis for the determination of cardiomyocyte size was performed as previously described.⁷⁶ In brief, cells were washed (PBS) and fixed with paraformaldehyde. Staining was performed with anti-sarcomeric α -actinin antibody (Sigma-Aldrich, #A7811), followed by secondary antibody incubation (Thermo Fisher, #A-11032). Additionally, nuclei were stained with DAPI (Thermo Fisher). Automated image acquisition was performed using the IN Cell Analyzer platform (GE Healthcare), followed by high-throughput cell detection and automated cardiomyocyte cell size measurement.

Adipocyte treatment and glycerol measurement

Differentiated adipocytes from the stroma vascular fraction were treated with the indicated doses of recombinant protein (for providers, see above) for 24h. The media was collected and glycerol was measured using the Free Glycerol Reagent (Sigma-Aldrich, #F6428) according to the protocol of the manufacturer. Glycerol was normalized to the protein content of the adipocytes of each well.

Neutralizing antibody treatment of myotubes

Treatment media (Calcium-free DMEM, 1% Pyruvate, 1% L-Glutamine, 1% FBS) was supplemented with 1% plasma from C26-tumor bearing mice and pre-incubated with the indicated concentrations of anti-LBP (#MAB6635, R&D Systems) anti-ITIH3 (# 21247-1-AP, Thermo Fisher Scientific), anti-IGFBP1 (#MAB675, R&D Systems) or the respective isotype control (rat IgG #6-001-F, mouse IgG #MAB002R or rabbit IgG #AB-105-C) for 20 minutes. The mix was used to treat differentiated myotubes for 48 hours, the media was refreshed after 24 hours. Myotubes were fixed and processed for imaging and analysis of myotube diameter as described above.

QUANTIFICATION AND STATISTICAL ANALYSIS

Processing and analyses of RNA-seq data

Processing and analyses of RNA-seq data For RNA-seq libraries, the STAR aligner (v2.4.2a)⁵⁷ was used for split-read alignment against the mouse genome assembly mm10 and UCSC knownGene annotation. Quantification of the number of mapped reads of each gene was performed using iRNA-seq (v1.1)⁵⁸ specifying the “-count gene” option. DESeq2 (v1.24.0)⁵⁹ was used to identify differentially expressed genes (Padj < 0.05) between one or more conditions within one or both of the C26/NC26 experiments in either the IP (hepatocyte) or input (whole liver) fraction. A set of expressed genes were defined as genes having a mean expression above 1 read per kb in at least one experimental condition, and from this group, a group of non-regulated genes were defined as having Padj > 0.5 in all pairwise comparisons. All genes regulated between one or more of the conditions were subjected to k-means clustering using 9 clusters and the “average” clustering method. A list of predicted secreted proteins were downloaded from Uniprot.org and intersected with the gene list from each cluster to identify potential cachexia regulated hepatokines. For cluster 3, a set of top candidates were defined based on consistent regulation (>8-fold relative to PBS) in both cachexia models (C26 and 8025).

Analyses of public RNA-seq data

Raw counts of RNA-seq data from healthy mice with hepatocyte-specific deficiency of both REV-ERB α and REB-ERB β ²⁹ were downloaded from GEO (GEO: GSE143524). DESeq2 (v1.24.0)⁵⁹ was used for normalization and estimation of Log2FCs. These data were merged with individual gene clusters to evaluate the effect of REV-ERB deletion at ZT10. Normalized count data were further used to illustrate the diurnal regulation of core clock genes in healthy WT mice. For the identification of REV-ERB-regulated secreted candidates from cluster 3, count data from control and KO animal at ZT7, ZT10, and ZT13 were extracted and analyzed combined across timepoints using a one-sided Wilcoxon test.

Pathway analysis

For functional annotation of differential gene expression results we performed an overrepresentation analysis (ORA) using the R package “clusterProfiler” (version 4.6.2).⁶⁰ As universe, we defined the genes showing expression with an average normalized count above one read per kb in at least one experimental condition as described above. Enrichment of differentially expressed genes was calculated with the “enrichGO” function using the ontology biological process (BP) of GO. Results were considered significant having both *p*-values < 0.05 and *q*-values < 0.1. Significant enrichment results were further analyzed for their semantic similarity with the R package “GOSemSim” (version 2.24.0).⁶¹ Pairwise similarities were computed with the implemented “Wang” method and the obtained similarity matrix was used for clustering by kmeans with *k*=3. The terms with smallest enrichment *p*-value (liver dataset) or the shortest description out of the top two results (heart dataset) was used as representative for each cluster and visualized as dotplot in clusterProfiler. All GO-terms for the liver and the heart can be found in [Tables S4](#) and [S5](#).

Upstream Regulator Analysis

The R implementation of the NicheNet algorithm (“NicheNetR”; version 2.0.0)²⁴ was used with the latest prior model (v2) to infer potential ligands that contribute to the observed transcriptional responses. Thereby ligands were not filtered for expression in sender cells but all ligands contained in the database were used as input for NicheNet. Thus, we did not interrogate specific sender-receiver cell interactions but aimed for an unbiased view on potentially active ligands that are associated with our cachexia models. In a first step, all gene clusters based on the two different suspected cellular backgrounds were aggregated into two metaclusters (GC1_GC6 resembling hepatocytes and GC7_GC9 non-parenchymal cells). We computed NicheNet’s ligand activity analysis for the concatenated regulated target genes and the respective metacluster backgrounds using the top 250 targets based on prior information. For both backgrounds the top 75 ligands were prioritized using the parameter “pearson”. With those top-ranked ligands the strongest ligand-target links were inferred for each individual gene cluster on the a priori model. From all obtained ligand-target connections we again filtered the top 75 links and visualized them in circus plots using the R package “circlize”.⁶⁷

Processing and analyses of ATAC-seq data

Sequence tags from ATAC-seq libraries were aligned to the mm10 using the BWA aligner (v0.7.5a-r405).⁶² Post-alignment processing of reads was performed with SAMtools (v0.1.19-44428cd)⁶³ by removing duplicate reads and filtering for high quality reads using SAMtools view using the following settings “-b -h -f 1 -F 4 -F 8 -F 256 -F 2048 -q 30”. Furthermore, we only used reads with a fragment length < 100bp, corresponding to the reads located in nucleosome-free regions. ATAC seq peaks were identified, annotated and tags in peaks were counted using HOMER (v4.10).⁶⁴ For visualization purposes, the individual tag directories of one condition were merged into one and bedgraphs were generated using HOMER makeUCSCfile specifying ‘-fragLength 70’ and ‘-fsz 20e’. Screenshots were generated using the UCSC genome browser.⁶⁶ For identification of accessible chromatin regions, peaks were called in each library with HOMER findPeaks using the following settings: ‘peaks’, ‘-fragLength 70’, ‘-style factor’, ‘-minDist 140’, ‘-size 70’. For all peak files, overlapping peaks were merged and collected in one master peak file. Tags were then counted in a 400 bp window around the peak centers for each individual library in the resulting master peak file. From this peak file mitochondrial peaks were removed, and high confident peaks were identified as having at least 30 tags per 400 bp window in all 3–4 replicates for one or more of the conditions. Dynamic enhancers were defined using DESeq2⁵⁹ as ATAC-seq peaks regulated between one or more conditions within one or both of the C26/NC26 experiments (*padj* < 0.05) and subjected to k-means clustering using 4 clusters and the “average” clustering method. Enhancer-gene cluster proximity was determined using bedtools to quantify the number of ATAC-peaks from each enhancer cluster within 20 kb of the TSS of genes in each gene cluster. For each gene cluster, a log2FC-enrichment was determined relative to a gene group not regulated between any conditions as defined above.

Transcription factor motif activity and targets

To compute the relative contribution of transcription factor motifs to enhancer activity and gene expression in a given condition, we used IMAGE (v1.1) that applies a motif response analyses approach to integrate enhancer (ATAC-seq) and gene expression (RNA-seq) activities.²⁶ We calculated the activity of a particular motif for a given sample by estimating the average contribution of that motif to the activity of all enhancers (Step1, Enhancer_activity) and expression of all expressed genes (Step 2, Gene_Activity). Since one ATAC-library failed quality control, average counts of the remaining three replicates of the PBS condition of the 8025 experiment was used in step 1. Dynamic motifs were defined as Gene_activities (Step 2) regulated between one or more conditions within one or both of the C26/NC26 experiments using an unpaired two-tailed Student’s *t* test corrected by the Benjamini & Hochberg method (*padj* < 0.05). This test was further used to estimate average and SEM of the change in activity relative to the respective PBS group.

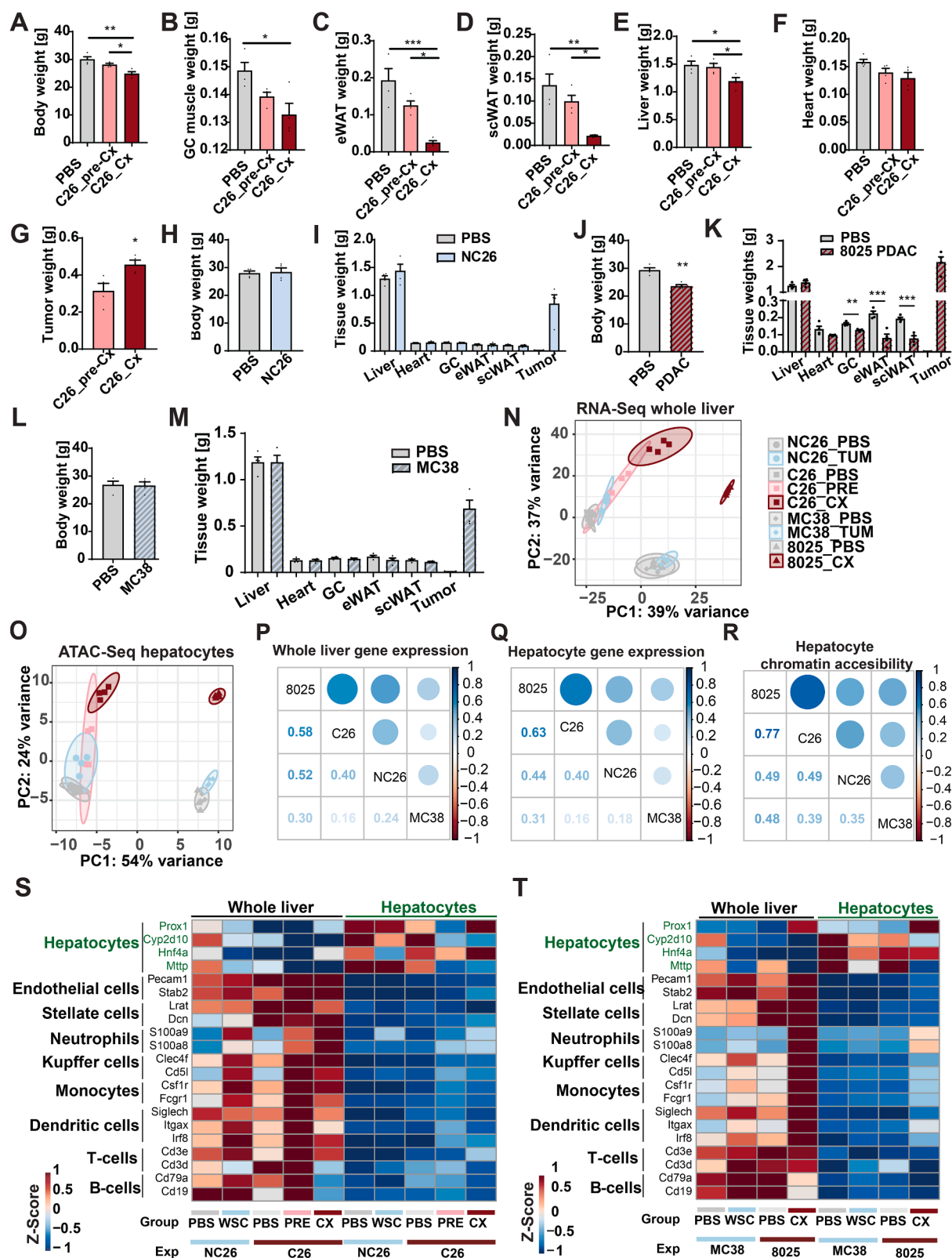
The resulting list of dynamic motif activities was subjected to k-means clustering using four clusters and the “average” clustering method. We also used IMAGE to predict target sites and target genes for the RORC and NR1D2 motifs. To investigate the significance of overlap between predicted target genes and hepatocyte gene clusters, the Fisher’s exact test was used for determination of the odds ratio and the 95% confidence interval.

Statistics

Unless stated otherwise, results from biological replicates were expressed as mean \pm standard error of the mean. Statistical analysis of non-sequencing data was performed using GraphPad Prism 7 and 9. To compare two conditions, unpaired Student’s t-tests (with or without Welch correction) or Mann–Whitney tests were performed. One-way analysis of variance (ANOVA) or Kruskal–Wallis tests with Šidák’s, Tukey’s or Dunn’s post hoc test were used to compare more than two groups. Spearman correlations were performed to test correlation between two variables. Statistical analysis of sequencing data was performed with R (4.2.3).⁷⁸ Enrichment of IMAGE-predicted target genes (Figure 3C) has been computed with Fisher’s exact test. Resulting odds ratios and 95% confidence intervals are reported.

Expression changes in response to hepatocyte-specific Nr1d1/2 knockout (Figure 3D) have been tested for shifting the log₂FCs of affected genes to values > 0 by using a one sided and one sample Wilcoxon test with $\mu=0$. Affected genes were determined by intersecting differentially regulated genes from public dataset of REV-ERB α/β deficient hepatocytes (GEO: GSE143524)²⁹ with cluster genes. Log₂FC from the dataset is reported and individually analyzed based on the cluster membership of the gene as shown in Figure 1D. For comparison of experimental groups in liver/hepatocyte nuclei and heart tissue based on changes in gene expression (Figures S2A and S3J), ATAC-seq tags (Figure S2D), and transcription factor motif activities (Figure S2F) we used the non-parametric Friedman test (similar to the parametric repeated measures ANOVA) with post-hoc analyses. We show post-hoc analyses of selected pairwise group comparisons based on all log₂FC or delta motif activities for each identified cluster. Computation was done using a published function (<https://www.r-statistics.com/2010/02/post-hoc-analysis-for-friedmans-test-r-code/>). No power calculations were used to predetermine sample sizes.

Supplemental figures



(legend on next page)

Figure S1. Characterization of mouse models of weight-stable cancer and CCx, related to Figure 1

(A–G) Body weights (A) and tissue weights (B–G) of HEP-INTACT BALB/c mice that were subcutaneously implanted with C26 colon cancer cells and sacrificed at a pre-cachectic state (C26_pre-Cx, no significant body weight loss) and cachectic state (C26_Cx $\geq 10\%$ body weight loss). Control mice received a PBS injection ($n = 4/\text{group}$, ANOVA with Šidák's multiple comparisons test for A–E, two-tailed t test for G).

(H and I) Body weights (H) and tissue weights (I) of HEP-INTACT BALB/c mice that were subcutaneously implanted with NC26 colon cancer cells that give rise to a tumor that does not induce weight loss. Control mice were injected with PBS ($n = 4/\text{group}$).

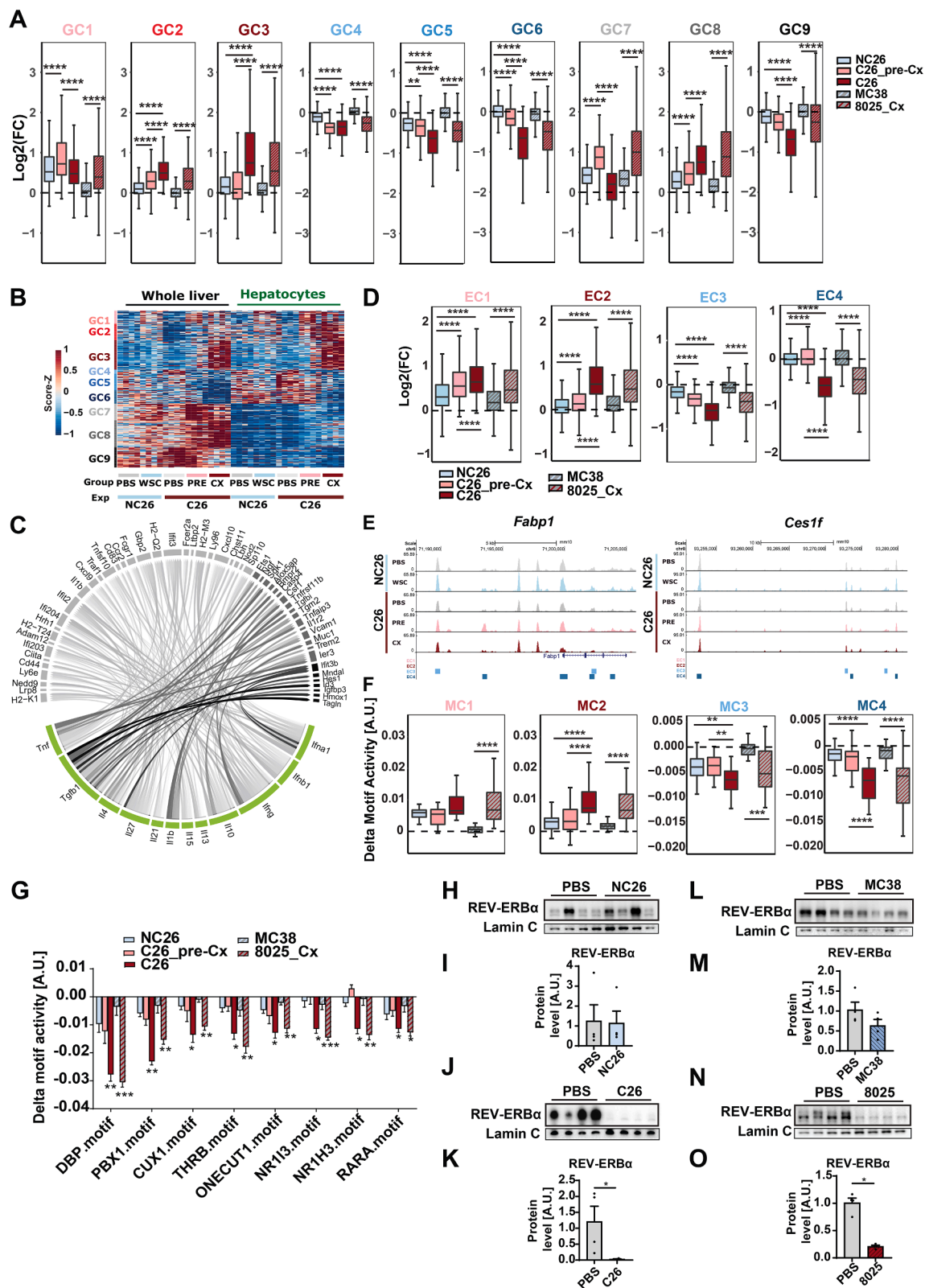
(J and K) Body weights (J) and tissue weights (K) of HEP-INTACT C57BL/6N mice that were orthotopically implanted with 8025 pancreatic ductal adenocarcinoma (PDAC) cells. Control mice received an PBS injection ($n = 4/\text{group}$, two-tailed t test for pairwise comparisons).

(L and M) Body weights (L) and tissue weights (M) of HEP-INTACT C57BL/6N mice that were subcutaneously implanted with MC38 colon cancer cells that give rise to a tumor that does not induce weight loss. Control mice were injected with PBS ($n = 4/\text{group}$). Error bars indicate standard error of the mean; $*p < 0.05$, $**p < 0.01$, $***p < 0.001$.

(N and O) PCA Analysis of RNA-seq data of whole-liver (N) and ATAC-seq data (O) of hepatocytes ($n = 4/\text{group}$). NC26_PBS, C26_PBS, MC38_PBS, 8025_PBS represent non-tumor-bearing PBS-injected control to the respective tumor model. TUM, tumor.

(P–R) Heatmaps illustrating correlation between changes in whole-liver gene expression (P), hepatocyte gene expression (Q), or hepatocyte chromatin accessibility (R) induced by different tumor models. The Pearson correlation of log2 foldchanges relative to PBS are depicted.

(S and T) Heatmaps showing average expression of marker genes for major hepatic cell types in whole-liver or hepatocyte nuclei from BALB/c models (S) or C57BL/6N models (T). CX, cachexia; WSC, weight-stable cancer.



(legend on next page)

Figure S2. Temporal dynamics of the hepatic transcriptome in cancer cachexia, related to Figures 1 and 2

(A) Boxplots showing log₂FC in gene expression for each of the GCs defined in Figure 1D. Log₂FC is calculated relative to PBS-injected mice for each of the indicated tumor models. Depicted log₂FC for all genes included in the clusters was based on $n = 4$ biological replicates. Error bars indicate 1.5 times of the inter-quartile range.

(B) Heatmap showing row-scaled expression of genes encoding secreted proteins within the individual GCs defined in Figure 1D.

(C) NicheNet analysis of ligand-target connections in whole-liver nuclei during cachexia. $^{**}p < 0.01$, $^{****}p < 0.0001$.

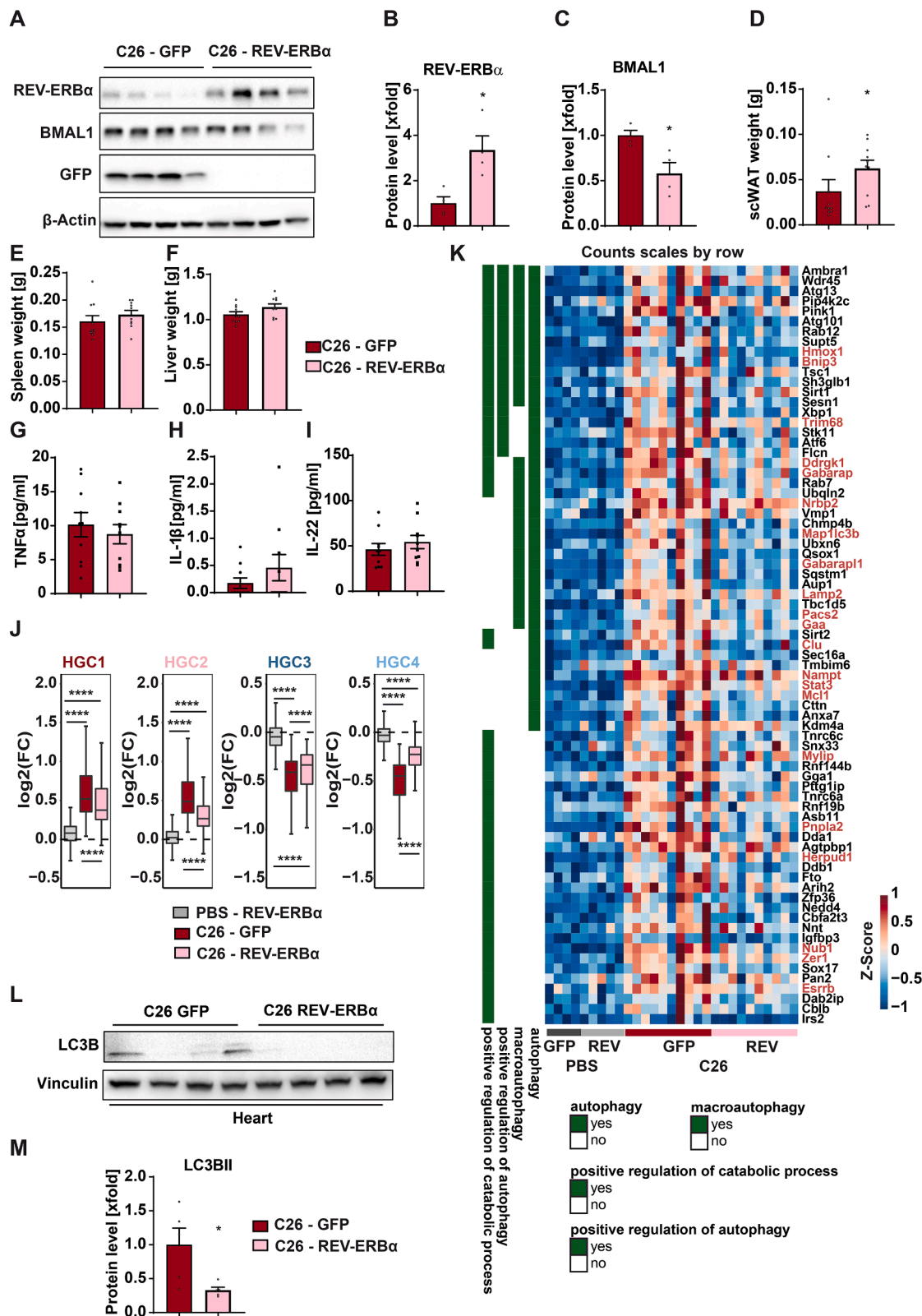
(D) Boxplots showing log₂FC in ATAC-seq tag counts for each of the enhancer clusters (ECs) defined in Figure 2A. Log₂FC is calculated relative to PBS-injected mice for each of the indicated tumor models. Error bars indicate 1.5 times of the inter-quartile range.

(E) USCS genome browser screenshots showing ATAC-seq read density in the fatty-acid-binding protein 1 (*Fabp1*) and carboxylesterase 1F (*Ces1f*) locus in GFP+ nuclei from HEP-INTACT mice. Average profiles ($n = 3-4$) of the indicated conditions are shown.

(F) Boxplots showing changes in motif activity (relative to PBS) for each of the motif clusters defined in Figure 2D. Delta activity was calculated relative to PBS-injected mice for each of the indicated tumor models. Error bars indicate 1.5 times of the inter-quartile range.

(G) Averaged changes in motif activity (relative to PBS) for the top 8 predicted transcription factors with cachexia-repressed motif activities in motif cluster 4 ($n = 4$ /group). Error bars indicate standard error of the activity-difference estimated with Student's *t* test.

(H-O) Western blot and protein quantifications of REV-ERB α of hepatic nuclear extracts of INTACT mice ($n = 4$ /group, error bars indicate standard error of the mean, Mann-Whitney test). Statistic tests for (A), (D), and (F) are described in the STAR Methods section. $^{*}p < 0.05$, $^{**}p < 0.01$, $^{***}p < 0.001$, $^{****}p < 0.0001$. CX, cachexia; WSC, weight-stable cancer.



(legend on next page)

Figure S3. Restoring liver REV-ERB α expression in C26 tumor-bearing mice ameliorates features of cachexia, related to Figure 4

(A–C) Confirmation of protein expression of REV-ERB α , BMAL1 and GFP in liver lysates of C26 tumor-bearing mice that received the control AAV expressing GFP or REV-ERB α (A) and subsequent quantification of REV-ERB α (B) and BMAL1 (C) protein levels using ImageLab ($n = 4$ /group, Mann-Whitney test).

(D–F) Weights of subcutaneous white adipose tissue (scWAT) (D), spleen (E), and liver (F) ($n = 10$ /group, Mann-Whitney test was used in D).

(G–I) Serum levels of indicated cytokines ($n = 10$ /group).

(J) Overall expression changes in heart GCs (HGCs) 1–4 compared with PBS-injected GFP control mice. Error bars indicate 1.5 times of the inter-quartile range.

(K) Heatmap displaying expression changes in heart tissue of genes included in GO-terms for “autophagy,” “macroautophagy,” “positive regulation of autophagy,” and “positive regulation of catabolic process.” All genes are significantly ($p_{\text{adj}} < 0.05$) upregulated in C26 tumor-bearing mice of GFP controls. Genes that are significantly downregulated ($p_{\text{adj}} < 0.05$) upon REV-ERB α overexpression are highlighted in red.

(L and M) Protein levels of LC3B in heart lysates of C26 tumor-bearing mice and subsequent quantification of LC3BII ($n = 5$ /group, Mann-Whitney test). Statistic tests for (J) are described in the [STAR Methods](#) section. $*p < 0.05$, $**p < 0.01$, $***p < 0.001$.

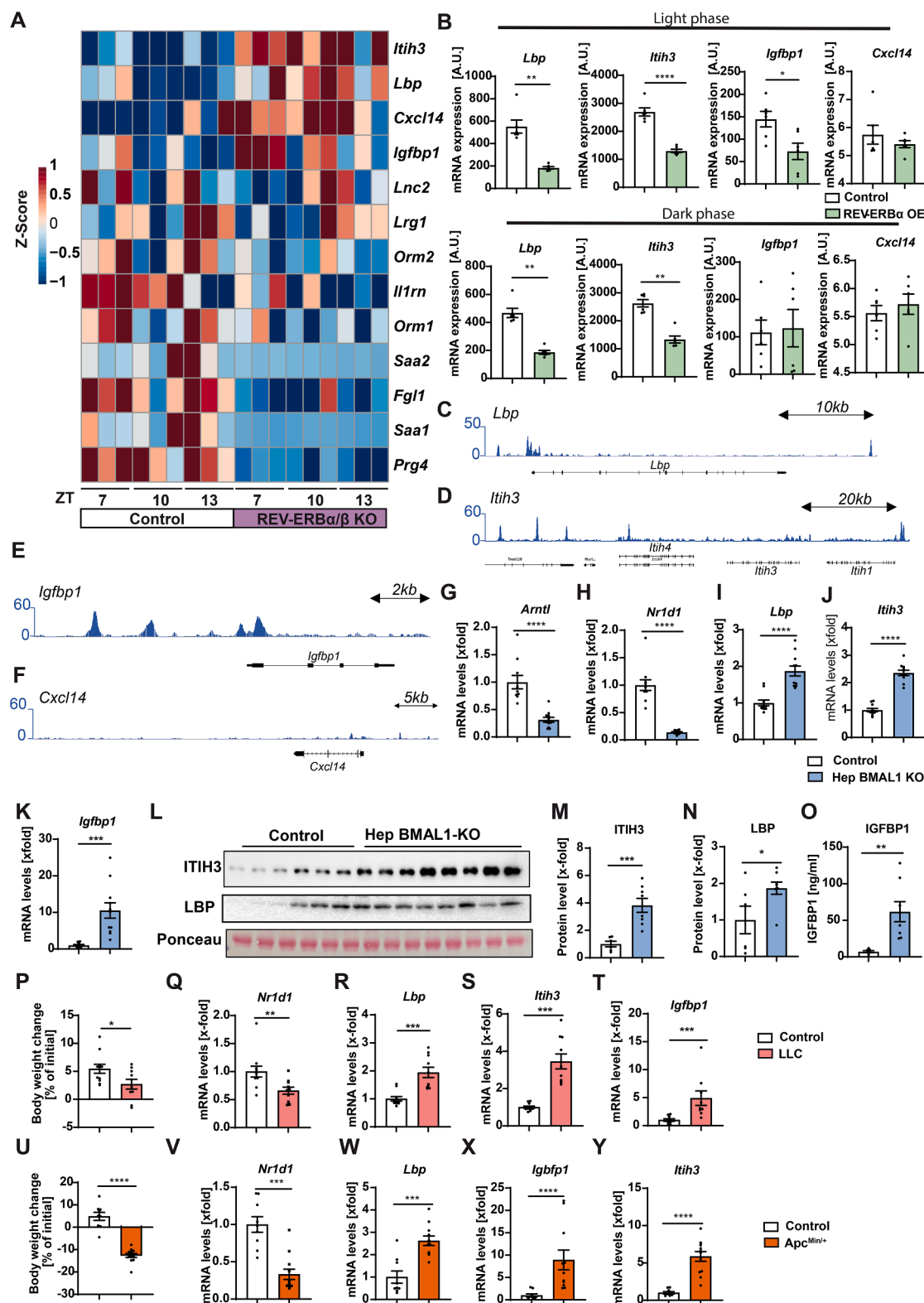


Figure S4. REV-ERBa/β deficiency associates with increased expression of specific hepatokines, related to Figure 5

(A) Liver mRNA levels of candidate genes in hepatocyte-specific REV-ERBa/β KO mice ($n = 4$ mice/group). Candidates were selected from genes encoding secreted proteins from gene cluster 3 (Figure 1F).

(legend continued on next page)

(B) Liver mRNA expression of candidate genes upon REV-ERB α overexpression in the light phase and dark phase ($n = 6$ /group, Mann-Whitney test for *Lbp* expression and *Itih3* expression in the dark phase. Remaining comparisons were analyzed using a two-tailed t test).

(C–F) Genome browser tracks showing genomic binding of REV-ERB α for *Lbp* (C), *Itih3* (D), *Igfbp1* (E), and *Cxcl14* (F) in mouse liver at zeitgeber time (ZT) 8. Left axis indicates normalized sequence-tag counts.

(G–K) mRNA expression of indicated genes in livers of hepatocyte BMAL1 knockout mice (Hep BMAL1 KO) ($n = 10$ – 11 /group, Mann-Whitney test was used for G–I, two-tailed t test for J and K).

(L–N), Western blot (L) for LBP and ITIH3 of plasma of Hep BMAL1-KO mice and quantification of protein levels (M and N, $n = 6$ – 8 /group, two-tailed t test with Welch correction was used for M, two-tailed t test was used for N).

(O) Circulating levels of IGFBP1 were determined by ELISA ($n = 7$ – 8 /group, two-tailed t test with Welch correction).

(P) Body weight change of Lewis lung carcinoma (LLC) tumor-bearing mice compared with control mice ($n = 10$ – 11 /group, two-tailed t test).

(Q–T) mRNA expression of indicated genes in livers of LLC tumor-bearing mice ($n = 9$ – 11 /group, Mann-Whitney test was used for Q, R, and T, two-tailed t test with Welch correction for S). Same values are shown for control groups as in (H)–(K) as common control groups were used.

(U) Body weight change of *Apc*^{Min/+} mice compared with control mice ($n = 9$ – 12 /group, two-tailed t test).

(V–Y) mRNA expression of indicated genes in livers of *Apc*^{Min/+} mice ($n = 9$ – 12 /group, Mann-Whitney test was used for V, W, and X, and a t test with Welch correction for Y). Error bars indicate standard error of the mean; * $p < 0.05$, ** $p < 0.01$, *** $p < 0.001$, **** $p < 0.0001$.

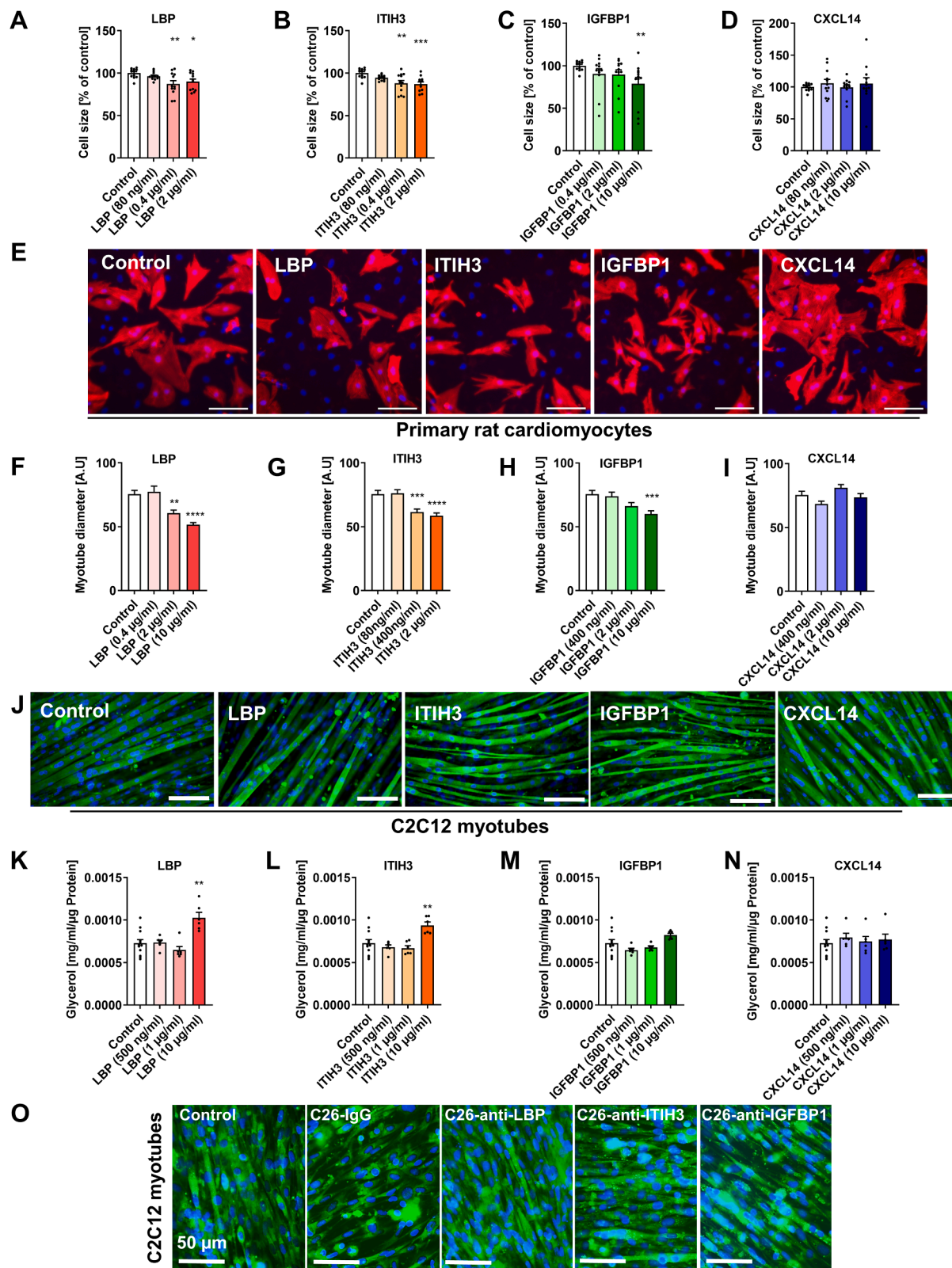


Figure S5. Liver-secreted factors induce catabolic processes *in vitro*, related to Figure 5

(A–D) Primary rat cardiomyocytes were treated with the indicated doses of LBP (A), ITIH3 (B), IGFBP1 (C) or CXCL14 (D) for 24 h and fixed with PFA ($n = 12/\text{group}$). Same values for the control column were used in (A)–(D).

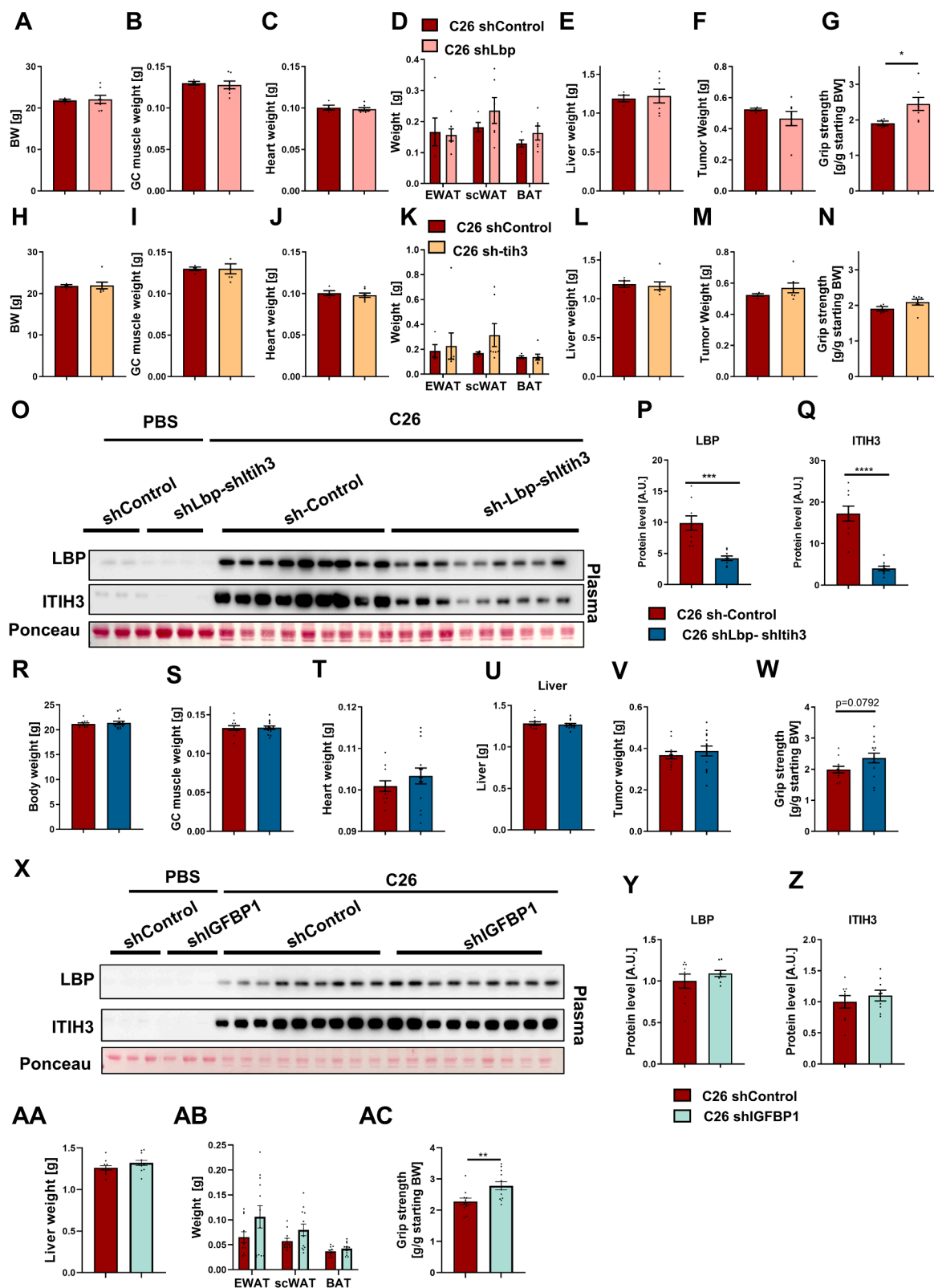
(E) Representative fluorescent images of primary rat cardiomyocytes that were treated with LBP (2 $\mu\text{g}/\text{mL}$), ITIH3 (2 $\mu\text{g}/\text{mL}$), IGFBP1 (10 $\mu\text{g}/\text{mL}$), and CXCL14 (10 $\mu\text{g}/\text{mL}$) for 24 h. Scale bar indicates 100 μm . Nuclei were stained with DAPI (blue) and cardiomyocytes with anti-sarcomeric α -actinin (red).

(F–I) C2C12 myotubes were treated with the indicated doses of LBP (F), ITIH3 (G), IGFBP1 (H), or CXCL14 (I) for 48 h and fixed with PFA. Wells were imaged and the myotube diameter was measured using ImageJ. Data are displayed as mean ($n \geq 55$ myotubes per condition) \pm SEM and representative of 3 independent experiments. Same values for the control column were used in (F)–(I).

(J) Representative fluorescent images of C2C12 myotubes that were treated with LBP (10 $\mu\text{g}/\text{mL}$), ITIH3 (2 $\mu\text{g}/\text{mL}$), IGFBP1 (10 $\mu\text{g}/\text{mL}$), and CXCL14 (10 $\mu\text{g}/\text{mL}$) for 48 h. Scale bar indicates 100 μm . Nuclei were stained with DAPI (blue) and myotube bodies with MitoTracker green (green).

(K–N) Differentiated adipocytes were treated with the indicated doses of LBP (K), ITIH3 (L), IGFBP1 (M) or CXCL14 (N) for 24 h. Glycerol content of the media as indicator for lipolysis was measured and normalized to the protein content of each well ($n \geq 6$ per condition). Same values for the control column were used in (K)–(N).

(O) Representative images of C2C12 myotubes that were treated with plasma (1%) of C26 tumor-bearing mice in combination with anti-LBP (5 $\mu\text{g}/\text{mL}$), anti-ITIH3 (20 $\mu\text{g}/\text{mL}$), anti-IGFBP1 (40 $\mu\text{g}/\text{mL}$) for 48 h. A representative IgG isotype control (IgG) image is shown. Scale bar indicates 50 μm . Error bars indicate standard error of the mean; ANOVA with Sidák's multiple comparisons test for (A), (B), and (L); Kruskal-Wallis test with Dunn's multiple comparisons test for (C), (F), (G), (H), and (K); ** $p < 0.01$, *** $p < 0.001$, **** $p < 0.0001$.



(legend on next page)

Figure S6. Knockdown of hepatokines ameliorates features of cancer cachexia *in vivo*, related to Figure 6

- (A) Final body weight upon *Lbp* knockdown in C26 tumor-bearing mice ($n = 4-7/\text{group}$).
- (B-F) Tissue weights upon *Lbp* knockdown in C26 tumor-bearing mice ($n = 4-7/\text{group}$).
- (G) Functional assessment of muscle function upon *Lbp* knockdown in C26 tumor-bearing mice using the grip strength test ($n = 4-7/\text{group}$, t test with Welch correction).
- (H) Final body weight upon *Itih3* knockdown in C26 tumor-bearing mice ($n = 4-7/\text{group}$). Values of control animals are the same as in (A).
- (I-M) Tissue weights upon *Itih3* knockdown in C26 tumor-bearing mice ($n = 4-7/\text{group}$). Values of control animals are the same as in (B)-(F).
- (N) Functional assessment of muscle function upon *Itih3* knockdown in C26 tumor-bearing mice using the grip strength test ($n = 4-7/\text{group}$,). Values of control animals are the same as in (G).
- (O-Q) Western blot for LBP and ITIH3 from plasma (O) upon combined *Lbp* and *Itih3* knockdown in C26 tumor-bearing mice and quantification of protein levels (P and Q, $n = 9/\text{group}$, t test with Welch correction).
- (R) Final body weights upon combined *Lbp* and *Itih3* knockdown in C26 tumor-bearing mice.
- (S-V) Tissue weights upon combined *Lbp* and *Itih3* knockdown in C26 tumor-bearing mice ($n = 11-14/\text{group}$).
- (W) Functional assessment of muscle function upon combined *Lbp* and *Itih3* knockdown in C26 tumor-bearing mice using the grip strength test ($n = 11-14/\text{group}$, two-tailed t test).
- (X-Z) Western blot for LBP and ITIH3 from plasma (X) upon *lgfbp1* knockdown in C26 tumor-bearing mice and quantification of protein levels (Y and Z, $n = 9/\text{group}$).
- (AA and AB) Tissue weights upon *lgfbp1* knockdown in C26 tumor-bearing mice ($n = 11-12/\text{group}$).
- (AC) Functional assessment of muscle function upon *lgfbp1* knockdown in C26 tumor-bearing mice using the grip strength test ($n = 11-12/\text{group}$, two-tailed t test). Error bars indicate standard error of the mean; * $p < 0.05$, ** $p < 0.01$, *** $p < 0.001$, **** $p < 0.0001$.

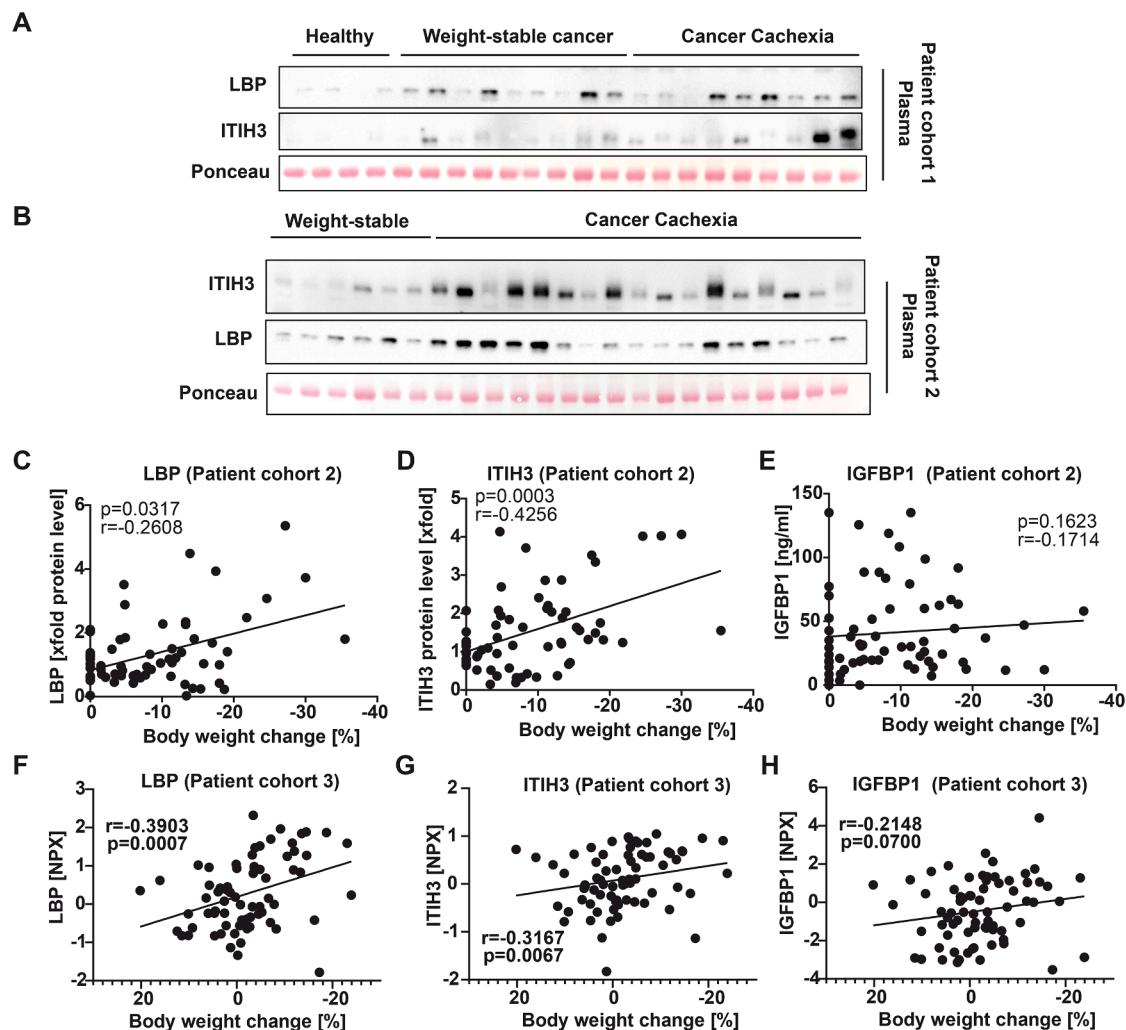


Figure S7. Hepatocyte-secreted factors are increased in cachectic cancer patients, related to Figure 7

(A) Representative western blot of LBP and ITIH3 in serum of individuals of patient cohort 1. Quantification of protein levels is shown in Figure 7.
(B) Representative western blot of LBP and ITIH3 in serum of individuals of patient cohort 2. Quantification of protein levels is shown in Figure 7.
(C–E) Correlation of circulating levels of LBP (C), ITIH3 (D), and IGFBP1 (E) with the observed changes in body weight of patient cohort 2.
(F–H) Correlation (Spearman) of circulating levels of LBP (F), ITIH3 (G), and IGFBP1 (H) with the relative changes in body weight of patient cohort 2.